

Recent Advances in Polarization-Encoded Optical Metasurfaces

Fei Ding,* Shiwei Tang,* and Sergey I. Bozhevolnyi

In recent years, optical metasurfaces, i.e., surface-confined arrays of engineered nanostructured elements (meta-atoms), have become an emerging research area due to their unprecedented capabilities of manipulating light with subwavelength spatial resolutions. The metasurfaces revolutionize thereby conventional bulky optics with compact planar elements. As the polarization is one of the intrinsic properties of light and of crucial importance for fundamental sciences and practical applications, the polarization-encoded functional optical metasurfaces featuring compactness, integration compatibility, and multiple functionalities have been in the focus of intensive research and development. Herein, the basic principles and emerging applications of polarization-encoded functional metasurfaces operating in the optical range are reviewed. Starting with the description of different polarization states, the review proceeds with considerations of how to interconvert and detect the state of polarization. The main achievements in polarization-multiplexing metasurface components (metadevices) are then summarized. Finally, a personal outlook on potential directions in this fast-growing research area is provided in the conclusions.

With polarization optics, such as polarizers and wave plates, unpolarized light with randomly oriented vibrations is transformed into either a linear, circular, or elliptical light wave. However, conventional optical components that allow to manipulate the state of polarization (SOP) are usually based on the accumulated phase retardation between two orthogonally polarized electric fields when light propagates a distance much larger than its wavelength.^[1] As a consequence, traditional polarization optics are bulky, thereby limiting the potential of miniaturization and dense integration in advanced photonic devices and systems. Therefore, it is highly desired to fully manipulate the SOP with a truly compact device that possesses excellent performance and multiple functionalities.

In recent years, optical metasurfaces, the 2D inhomogeneous interface composed of planar meta-atoms, have shown their

unprecedented capabilities of controlling the optical fields with a subwavelength spatial resolution at the single meta-atom level.^[2–12] Specifically, the phase, amplitude, and even frequency of light can be tailored at will through judiciously designed meta-atoms with particular responses. As a result, optical metasurfaces have gained much attention and started to replace conventional bulky optics with planar, compact, and high-performance meta-devices, especially for polarization optics.^[2–12] In particular, polarization-encoded metasurfaces exhibit the advantages of flexibility, versatility, ease of fabrication and integration.

Herein, we review the basic principles and emerging applications of polarization-encoded functional metasurfaces in the optical regime. We mainly focus our attention on the optical metasurfaces although there are many fantastic metasurface-enabled polarization converters and polarization-multiplexing devices in the microwave^[13–16] and terahertz regimes.^[17–19] After the description of polarization (Section 2), we introduce how to convert and detect the SOP of light with metasurfaces (Section 3 and 4). Then we summarize the main achievements in polarization-multiplexed metadevices (Section 5). Finally, we end up this review with a short conclusion and personal outlook on potential directions in this fast-growing research area (Section 6).

1. Introduction

Similar to frequency, phase, and amplitude, polarization is an intrinsic property of light. Generally, polarization describes the oscillation direction of the electric field and indicates the transverse nature of light.^[1] As polarization is uncorrelated with frequency, phase, and amplitude, it could extend the information channels and has been widely used in practical applications. However, the majority of light sources, such as the sun, emit unpolarized light with randomly oriented oscillation directions.

Prof. F. Ding, Prof. S. I. Bozhevolnyi
Centre for Nano Optics
University of Southern Denmark
Campusvej 55, DK-5230 Odense M, Denmark
E-mail: feid@mci.sdu.dk

Prof. S. Tang
School of Physical Science and Technology
Ningbo University
Ningbo 315211, China
E-mail: tangshiwei@nbu.edu.cn

 The ORCID identification number(s) for the author(s) of this article can be found under <https://doi.org/10.1002/adpr.202000173>.

© 2021 The Authors. Advanced Photonics Research published by Wiley-VCH GmbH. This is an open access article under the terms of the Creative Commons Attribution License, which permits use, distribution and reproduction in any medium, provided the original work is properly cited.

DOI: 10.1002/adpr.202000173

2. The Description of Polarization

In classical optics, the polarization of light is usually expressed mathematically in the vector form, such as the Jones vector^[20]

and Stokes parameters.^[21] If we consider a monochromatic z -propagating plane wave, the phase and amplitude of two orthogonal electric fields can be defined by the Jones vector or matrix

$$E = \begin{bmatrix} E_x \\ E_y \end{bmatrix} = \begin{bmatrix} A_x e^{i\varphi_x} \\ A_y e^{i\varphi_y} \end{bmatrix} \quad (1)$$

where A_x , A_y and φ_x , φ_y are the amplitudes and phases for two orthogonal components, respectively. However, the Jones vector cannot be applied to describe unpolarized or partially polarized light. To solve this problem, the Stokes parameters are introduced, which can fully determine the SOP and total intensity of any light. The Stokes parameters are often expressed into a vector and written as

$$S = \begin{bmatrix} S_0 \\ S_1 \\ S_2 \\ S_3 \end{bmatrix} = \begin{bmatrix} A_x^2 + A_y^2 \\ A_x^2 - A_y^2 \\ 2A_x A_y \cos \delta \\ 2A_x A_y \sin \delta \end{bmatrix} = \begin{bmatrix} I_x + I_y \\ I_x - I_y \\ I_a - I_b \\ I_r - I_l \end{bmatrix} \quad (2)$$

where $\delta = \varphi_y - \varphi_x$ is the relative phase difference between two electric fields and I_i represents the intensity in a specific polarization basis. From Equation (2), it is clear that Stokes parameters can be expressed with a set of intensities in different polarization bases. In particular, S_0 represents the intensity of light, whereas S_1 – S_3 describe the polarization state and are obtained by measuring the intensities of the two orthogonal components in three polarization bases, e.g., (\vec{x}, \vec{y}) , $(\vec{a}, \vec{b}) = (1/\sqrt{2})(\vec{x} + \vec{y}, -\vec{x} + \vec{y})$, and $(\vec{r}, \vec{l}) = (1/\sqrt{2})(\vec{x} + i\vec{y}, \vec{x} - i\vec{y})$. It is worth noting that S_1 – S_3 are usually normalized by S_0 , so that all possible values are within ± 1 . Given the close connection between the SOP and Stokes parameters, it is obvious that the SOP can be quickly determined once a device is capable of measuring the intensities of two orthogonal polarization states for all three bases.

3. Metasurface-Based Polarization Converters

3.1. Polarization Converters Based on Homogeneous Birefringent Metasurfaces

As mentioned in the previous section, any polarized light could be decomposed into orthogonal components in different bases, such as linearly polarized (LP) components along x - and y -directions. If one wants to change the SOP, it is necessary to control the phase and amplitude of two orthogonal LP components. Conventional polarization converters are constructed with birefringent materials, such as crystals, where the relative phase difference between two orthogonal linear components is gradually achieved during light propagation over a large distance. Therefore, the designed polarization converters suffer from bulky configurations and limited functionalities, going against the trends of minimization and integration in photonic devices and systems. These trends, in turn, boost the recent developments of metasurface-based polarization converters that could replace traditional bulky polarization converters due to their ultrathin planar configurations, excellent performance, and diverse functionalities.

To achieve polarization conversion with metasurfaces, the first method is to utilize homogeneous birefringent metasurfaces

made up of identical elements possessing different responses for two orthogonal LP components (e.g., E_x and E_y). In particular, each anisotropic meta-atom produces different amplitudes/phases for the reflected or transmitted fields. Generally, an anisotropic meta-atom with its two major axes positioned along x - and y -directions could be represented by a Jones matrix

$$M = \begin{bmatrix} M_{xx} & 0 \\ 0 & M_{yy} \end{bmatrix} \quad (3)$$

where M_{xx} and M_{yy} are the complex scattering coefficients for x - and y -polarized incident beams, determined by the meta-atom's dimensions along two main axes. If the amplitudes are equal ($|M_{xx}| = |M_{yy}|$) and the phase difference $\Delta\Phi = \Phi_{xx} - \Phi_{yy}$ (e.g., $\Phi_{xx} = \arg(M_{xx})$) is $\pi/2$ or π , functional quarter-wave plates (QWPs)^[22–27] or half-wave plates (HWPs)^[28–31] can be accordingly designed for the circularly or diagonally polarized wave, respectively. For instance, an array of single-layered meta-atoms that only support electric dipole resonances have been used to realize the QWP functionality as $\Delta\phi = \pi/2$ can be easily fulfilled.^[22,23,26] **Figure 1a** shows one typical example of periodic metallic nanorods functioning as a QWP, where the unit cell is composed of two silver (Ag) nanorods with orthogonal orientations.^[23] By optimizing the dimensions, detuned electric dipole resonances with similar dispersions could be achieved, thereby allowing for efficient circular-to-linear polarization conversion over a broadband range of wavelengths where the degree of linear polarization is remarkably large. However, this type of single-layered waveplates is typically constrained by limited conversion efficiencies given the unwanted scattering channels. To boost the efficiency and broaden the operation bandwidth, gap-surface plasmon (GSP) metasurfaces composed of an array of metallic meta-atoms, a subwavelength dielectric spacer, and a thick metal substrate,^[32] forming typical metal–insulator–metal (MIM) configurations, have been used to achieve high-efficiency waveplates.^[24,25,27–29] Jiang et al. demonstrated broadband waveplates with MIM configurations,^[29] where the dispersion of resonant metallic L-shaped antennas can be compensated by the intrinsic dispersion of the dielectric spacer with a specific thickness, thereby allowing for dispersion-free response and broadband polarization conversion. As shown in **Figure 1b**, the measured amplitude ratio remains unity for both the x - and y -polarized incidences with the measured reflectance above 0.85 in the spectrum ranging from 86 to 116 THz. Moreover, the phase difference is -90° for the x -polarized incident light. As such, the realized QWP could work in a broadband frequency range with a bandwidth approaching $\approx 30\%$ of the central frequency. In addition to the QWP, the wide-band HWP can be accordingly realized by optimizing the dimensions of MIM structures.

Although the efficiencies of MIM metasurface-based polarization converters have been increased to some extent, they are still suffering from reduced efficiencies when the working wavelength moves to the short range, for instance, near-infrared and visible regimes, due to the increased Ohmic loss. To address this issue, a hybrid birefringent metasurface has been proposed to achieve a broadband and highly efficient HWP at telecom wavelengths.^[30] **Figure 1c** schematically shows the hybrid metasurface that is composed of single-crystalline silicon (Si) bricks

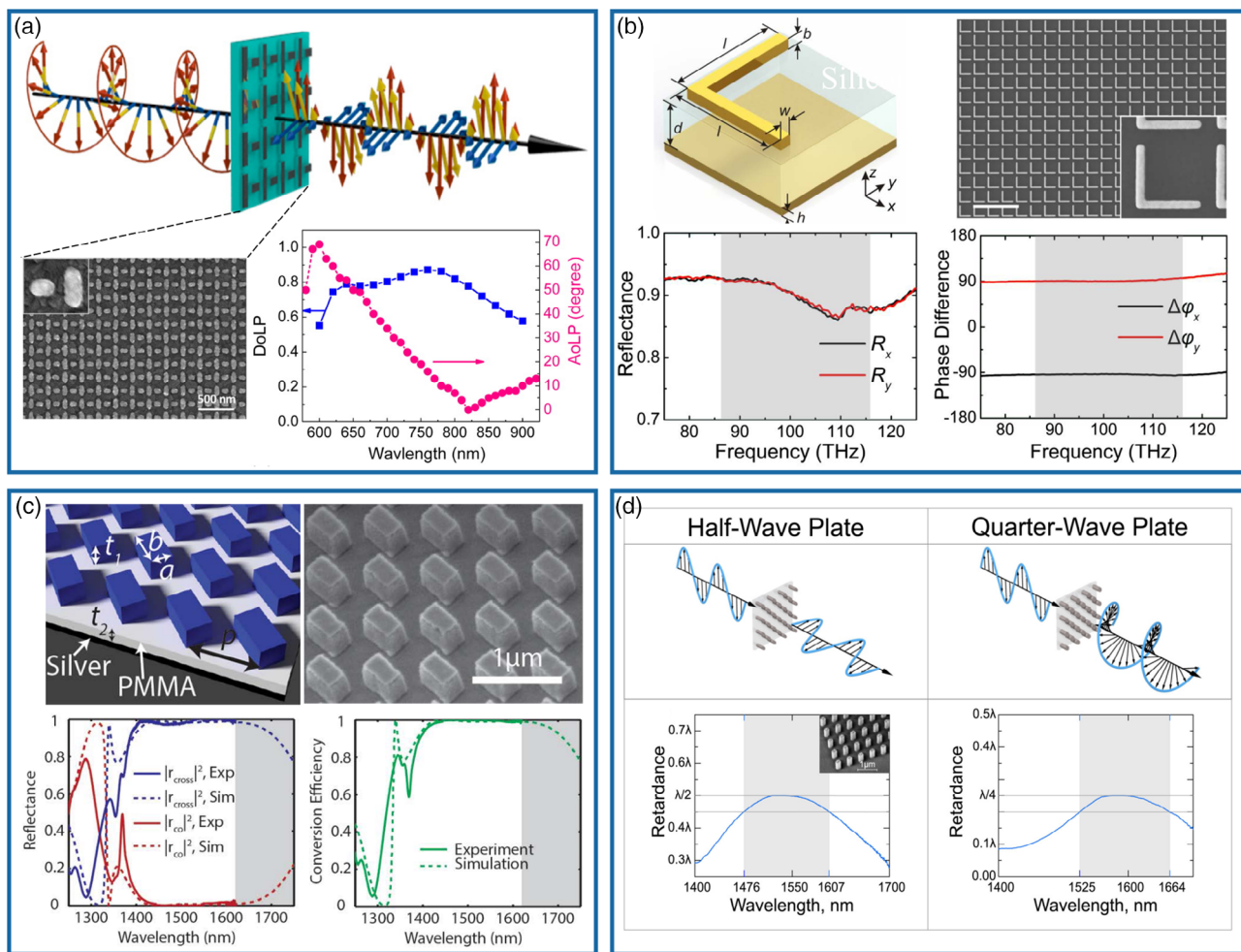


Figure 1. Polarization converters based on homogenous birefringent metasurfaces. a) Top panel: schematic of a metasurface QWP composed of plasmonic nanorods. Lower left panel: scanning electron microscope (SEM) image of part of the fabricated sample. Lower right panel: measurements of the degree of linear polarization and angle of linear polarization under CP excitation. b) Top left panel: MIM unit cell composed of an array of L-patterns on top of a dielectric spacer layer and a perfect electric conductor. Top right panel: field-emission SEM of the fabricated arrays with the scale bar of 5 μm . Lower left panel: experimentally measured reflectance for x- and y-polarized incident beams. Lower right panel: experimentally measured phase difference between x- and y-polarized light. c) Top left panel: dielectric metareflect array that functions as a near-infrared HWP. Top right panel: SEM image of the fabricated structure. Lower left panel: the measured and simulated reflectivities of the co- and cross-polarized light. Lower right panel: the measured and simulated polarization conversion efficiency. d) Top panel: schematic of all-dielectric metasurfaces for HWP and QWP in a broadband range. Lower panel: experimentally retrieved retardance of the HWP and QWP. a) Reproduced with permission.^[23] Copyright 2013, American Chemistry Society (ACS). b) Reproduced under the terms of Creative Commons Attribution (CC BY) license.^[29] Copyright 2014, The Authors, Published by American Physical Society (APS). c) Reproduced with permission.^[30] Copyright 2014, ACS. d) Reproduced under the terms of Creative Commons Attribution (CC BY) license.^[31] Copyright 2016, The Authors, Published by American Institute of Physics (AIP).

rotated with an angle of 45° and a Ag back-reflector separated by a dielectric spacer, hereby mimicking an MIM configuration. Due to the transparency of crystalline Si and the high reflectivity of Ag, the total loss can be considerably reduced in the near-infrared range. Impressively, the measured cross-polarized reflectivity remains above 97%, whereas the copolarized reflectivity is approaching 0 from 1420 to 1620 nm. The measured linear polarization conversion ratio exceeds 98% in the corresponding wavelength range across a 200 nm bandwidth. Similar to plasmonic counterparts, all-dielectric anisotropic meta-atoms composed of high-refractive index materials can be used to construct compact polarization converters.^[10] In particular, due to the existing

multipole Mie resonances that are spectrally overlapped at a single frequency or spectrum range with similar or identical strengths,^[10,33–35] independent and complete phase and polarization control of transmitted fields is possible. Meanwhile, the transmission efficiency can be boosted to a large extent by suppressing the reflection. The resulting retardation between two electric field components can be much higher than the propagation phase accumulated in birefringent crystals. As a result, the phase difference can be arbitrarily engineered by the dimensions and orientations, resulting in various all-dielectric metasurface converters in transmission mode with high efficiencies.^[10,31] Here, we would like to highlight a type of broadband dielectric

metasurfaces enabling high-efficiency polarization manipulation based on spaced Si nanopillars, as shown in Figure 1d.^[31] In this design, by overlapping the scattering profiles of dielectric and magnetic multipolar modes of the constitute Si meta-atoms, the generalized Huygens principle can be fulfilled, leading to the destructive interference of reflected fields in a broadband spectrum. Based on this design, highly efficient HWPs and QWPs that cover multiple telecom bands with $\approx 90\%$ transmission and $\approx 99\%$ polarization conversion ratio have been experimentally demonstrated. In particular, the birefringence Δn corresponding to a π phase difference is around 0.9 at $\lambda = 1550$ nm, which is much higher than the natural materials.

3.2. Polarization Converters Possessing Multiple Functionalities Based on Phase-Gradient Birefringent Metasurfaces

In addition to intrinsic functionality of polarization conversion (e.g., linear-to-circular conversion), metasurface-based polarization converters can be explored to integrate more complicated and diverse functionalities by spatially arranging several birefringent meta-atoms functioning as nanowaveplates. Various

metasurface-based polarization converters possessing additional functionalities have been accordingly demonstrated, such as beam-steering,^[36–39] focusing,^[37,39–43] vortex-beam generation.^[37,44–49] For example, Ding et al. have experimentally demonstrated a near-infrared background-free GSP HWP that combines functionalities of linear-to-linear polarization conversion and beam-steering in a compact metadvice.^[36] The background-free HWP consists of four different HWPs in a supercell that supplies a constant phase gradient for the reflected waves in cross-polarization, leading to anomalous reflection for cross-polarized reflected fields (Figure 2a). In the design, four anisotropic MIM meta-atoms that enable both efficient linear-polarization conversion and complete phase control over reflected fields have been designed with full-wave numerical calculations, which cover nearly 2π phase range for the cross-polarized reflected light. Therefore, copolarized and cross-polarized reflected waves can be separately distributed in space, greatly boosting the linear-polarization conversion ratio. In the experiment, the cross-polarized reflection is dominating, whereas the copolarized reflection is greatly suppressed, approaching zero. In addition, the power ratio between the cross-polarized and copolarized fields is larger than 20,

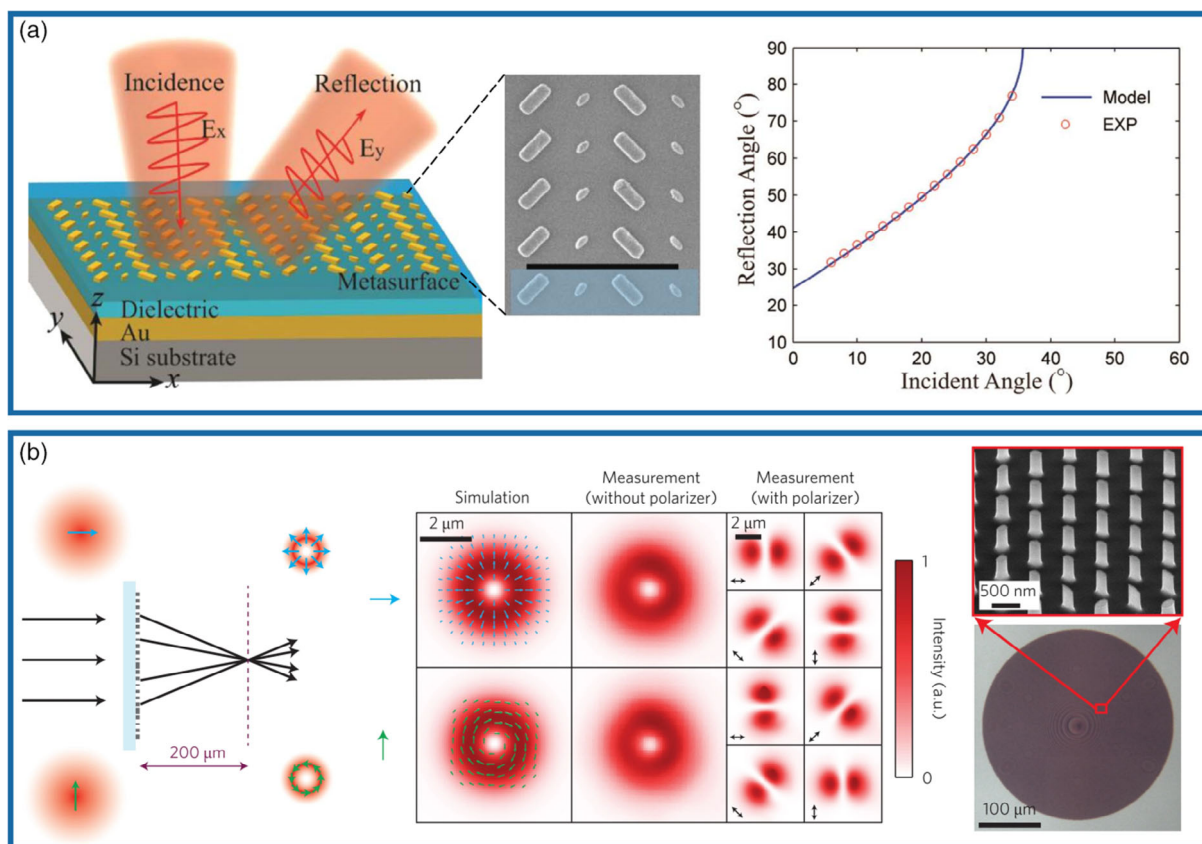


Figure 2. Polarization converters possessing multiple functionalities based on phase-gradient birefringent metasurfaces. a) Left panel: illustration of a reflective background-free HWP consisting of four antennas that provides a phase gradient for the polarization-converted reflected fields. Middle panel: SEM image of the fabricated sample. Right lower: measured and calculated anomalous reflection angle θ_r as a function of the incident angle θ_i at $\lambda = 1000$ nm. b) Left panel: illustration of a dielectric metasurface for focused radially (azimuthally) polarized light generation under x-polarized (y-polarized) excitation. Middle panel: simulated and measured intensity profiles. Right panel: optical microscope (bottom) and SEM (top) images of the device. a) Reproduced with permission.^[36] Copyright 2015, ACS. b) Reproduced with permission.^[37] Copyright 2015, Springer Nature.

indicating the enhanced capability of polarization conversion regardless of fabrication imperfectness. As shown in Figure 2a, the measured anomalous reflection angle θ_r follows the theoretical prediction with the varied incident angle θ_i . Following this strategy, multifunctional metadevices that enable linear-polarization conversion and focusing have also been exploited to produce various focused beams possessing distinct wavefronts, such as orthogonally polarized vortex beams.^[48]

As complementary to plasmonic polarization converters, dielectric metasurfaces have also been utilized for simultaneous polarization conversion and wavefront shaping with high efficiencies in transmission.^[10,37,40,41,43] For example, Faraon and coworkers utilized arrays of high-contrast Si elliptical meta-atoms to provide complete and independent control over polarization and phase simultaneously.^[37] Figure 2b shows a Si meta-device that allows to convert an x -polarized (y -polarized) Gaussian beam into a focused radially (azimuthally) polarized Bessel–Gauss beam. In this way, this metadvice can mimic the combined functionalities of a q-plate and a lens. Impressively, the measured transmission efficiencies can be higher than 85% for both the x - and y -polarizations, which are ascribed to the spectrally overlapped electric and magnetic resonances with equal strengths. Due to the flexibility of this dielectric metasurface platform, more complicated wavefronts can be achieved along with the polarization transformation.

3.3. Polarization Converters Based on Metasurfaces Consisting of Two Meta-Atom Subarrays

Although the aforementioned background-free HWP shows excellent performance at the design wavelength of $\lambda = 1000$ nm,^[36] its operation bandwidth is still limited as the metasurface bandwidth is made up from the bandwidths of four different meta-atoms, each functioning as an HWP and having its own intrinsic bandwidth. Generally, the bandwidth of metasurface-based waveplates is usually limited because the eigenmodes of meta-atoms are typically not wide enough. Once the metasurfaces work away from the optimized frequency, the amplitude ratio deviates from one and the phase difference is not π or $\pi/2$ anymore. To overcome this limitation, a QWP that features background-free and broadband performance was demonstrated by integrating two subunits of phased antennas with different dimensions and orientations in a supercell, which can work for any LP incident beam.^[50] Upon excitation with a LP wave, the two subunits comprising the QWP create two waves with same propagation directions, equal amplitudes, orthogonal polarization states, and a phase difference of $\pi/2$ controlled by the offset between two subunits (left panel in Figure 3a). These two copropagating beams will interfere and produce a circularly polarized (CP) extraordinary beam that is directed to a particular direction away from the ordinary beam. Therefore,

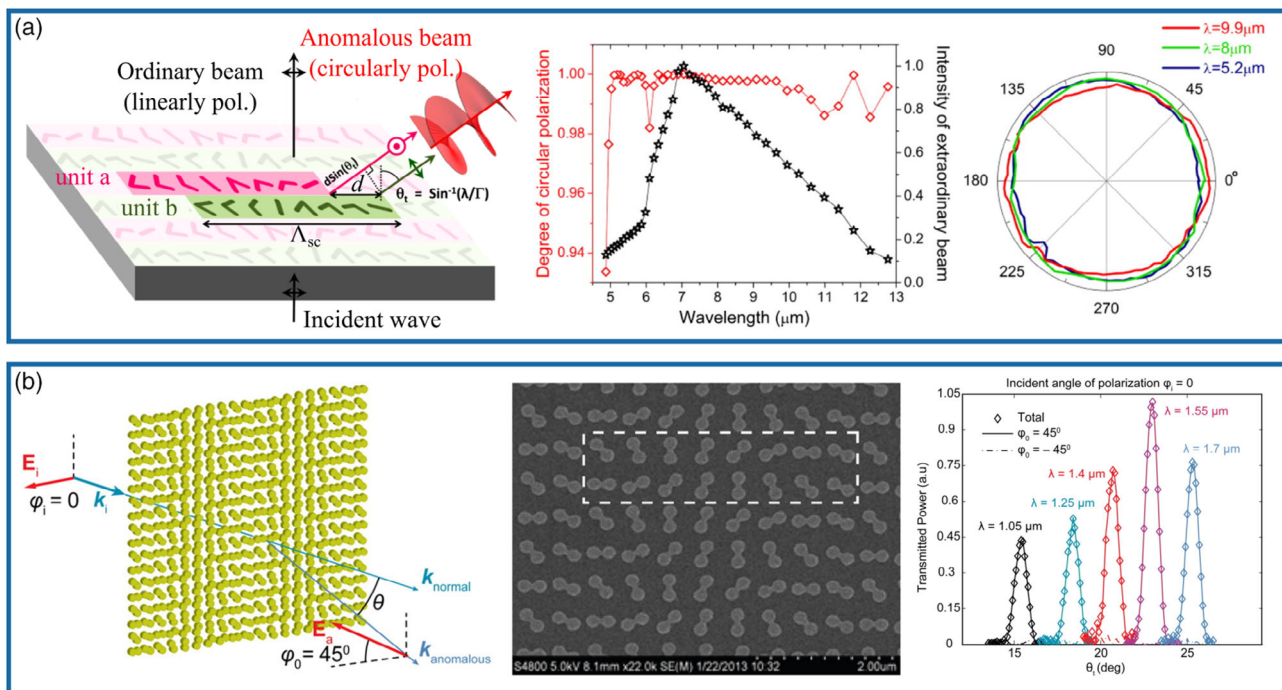


Figure 3. Polarization converters based on metasurfaces composed of two meta-atom subarrays. a) Left panel: illustration of a background-free metasurface QWP based on two V-shaped antenna subunits that generate two copropagating orthogonal LP waves with identical amplitudes and a constant phase difference of $\pi/2$ upon LP incidence. Middle panel: simulated degree of circular polarization and the beam intensity as a function of the wavelength. Right panel: measured SOPs of the extraordinary beam at $\lambda = 5.2, 8,$ and 9.9 μm by projecting the transmitted intensity with a linear polarizer in front of a detector. b) Left panel: working principle of a linear-polarization-rotation metasurface with two PB-phase subarrays orientated in opposite directions. Middle panel: SEM image of the fabricated sample. Right panel: measured transmitted power at different wavelengths, where the transmitted light is rotated by 45° with input angle of polarization $\varphi_i = 0$. a) Reproduced with permission.^[50] Copyright 2012, ACS. b) Reproduced with permission.^[51] Copyright 2014, ACS.

the calculated degree of circular polarization approaches unity in a broadband wavelength range from 5 to 12 μm , as shown in the middle panel of Figure 3a. In addition, the experimentally demonstrated suppression ratio between the intensities of the right circular polarization and left circular polarization is ≈ 700 at $\lambda = 8 \mu\text{m}$, indicating the excellent performance of linear-to-circular polarization conversion.

Similarly, arbitrary linear polarization rotation can be achieved with Pancharatnam–Berry (PB) or geometric phase metasurfaces consisting of spatially varied identical meta-atoms.^[51,52] The mechanism of PB phase can be well explained by the Jones matrix.^[2–12] Considering an anisotropic meta-atom rotated with an angle of θ with respect to the x -axis, its Jones matrix can be written as

$$M(\theta) = R(-\theta) \begin{bmatrix} M_{xx} & 0 \\ 0 & M_{yy} \end{bmatrix} R(\theta) \quad (4)$$

where M_{xx} and M_{yy} are the complex scattering coefficients of x - and y -polarized incident lights and $R(\theta) = \begin{bmatrix} \cos \theta & \sin \theta \\ -\sin \theta & \cos \theta \end{bmatrix}$ represents the rotation matrix. If the incident light is CP with $E_{\text{in}} = \begin{bmatrix} 1 \\ \pm i \end{bmatrix}$, the output light becomes

$$E_{\text{out}} = M(\theta) E_{\text{in}} \\ = \frac{M_{xx} + M_{yy}}{2} \begin{bmatrix} 1 \\ \pm i \end{bmatrix} + \frac{M_{xx} - M_{yy}}{2} \exp(\pm i2\theta) \begin{bmatrix} 1 \\ \mp i \end{bmatrix} \quad (5)$$

where the first term stands for the spin-maintained CP light, whereas the second term describes the CP light with the opposite spin to the incident light that gains a PB phase of $\pm 2\theta$. From Equation (5), it is clearly observed that full 2π phase coverage can be easily realized for the cross-polarized CP wave by rotating the meta-atom from 0° to 180° . Also, the additional PB phase is spin-conjugated, making it possible to implement spin-dependent multiplexed phase profiles, which can be used to realize broadband and background-free waveplates. Figure 3b shows an optically active metasurface composed of nonchiral metallic nanoantennas, which can rotate LP light by 45° in a broadband near-infrared spectrum range.^[51] The metasurface consists of two PB phase subarrays with an offset, splitting two CP beams in opposite directions, where left CP (LCP) and right CP (RCP) components can interfere together to form a LP beam. Specifically, the rotation angle of the LP output beam φ_0 can be accurately controlled by changing the offset d between two subarrays and the periodicity p

$$\varphi_0 = 180^\circ \times \frac{d}{p} \quad (6)$$

From Equation (6), it should be noted that this optical activity is quite robust to the fabrication imperfections, such as the uncertainties of the optical constants of deposited materials. Once the offset d is equal to $p/4$, two anomalously transmitted beams with a rotation angle of 45° are deflected in opposite directions, whereas a copolarized output beam is directly transmitted. As the design is based on PB phase with one identical meta-atom, this polarization rotation effect is quite broadband. However, the

output power in the desired anomalous beam becomes lower and lower when the device is working away from the optimal wavelength. It should be noted that the efficiency of such a design is only about 4%. To enhance the efficiency, MIM metasurfaces and dielectric metasurfaces that function as HWPs with $M_{xx} + M_{yy} = 0$ should be utilized.^[9,10] Therefore, the copolarized component will disappear and all power will go to the output beams with desired polarization states.

3.4. All-Polarization Converters Based on Metasurfaces

In the previous demonstrations, metasurface-based polarization converters are typically designed for a specific and single polarization transformation. For instance, a metasurface QWP can only achieve circular-to-linear or linear-to-circular polarization conversion. In practical applications, an ideal all-polarization converter that enables generating and manipulating arbitrary well-defined polarization states while maintaining the excellent properties of compactness, high-efficiency, wide bandwidth, ease of fabrication, and compatibility with nanophotonics. In recent years, a few examples of all-polarization converters based on optical metasurfaces have been implemented in both reflection^[52–55] and transmission modes.^[56–58] In 2017, Tsai's group demonstrated a GSP metasurface that produces reflected beams with six different polarization states (four linear polarizations and two circular polarizations) into different diffraction angles with a LP incident source (Figure 4a).^[52] Similar to the study by Shaltout et al.,^[51] two PB-phase subarrays composed of spatially orientated HWP meta-atoms are offset with different distances to form four types of supercells, corresponding to four different linear polarization states. At the same time, the PB-phase modulation of one single subarray is responsible for generating two circular polarization states. By replacing gold (Au) with aluminum (Al) to construct the topmost plasmonic antennas, the fabricated sample allows for broadband operation in the whole visible spectrum. However, the capability of wavefront engineering for the six output beams is limited. To circumvent this constraint, Deng et al. proposed the concept of diatomic metasurfaces and successfully demonstrated vectorial metaholography, namely holographic images containing several polarization states.^[53] The so-called metamolecule diatomic metasurface is composed of two orthogonally rotated meta-atoms with identical dimensions (Figure 4b). By changing the displacement and orientation of meta-atoms, both the phase and polarization can be manipulated at the oblique incidence, superior to previous approaches where the control over phase and polarization is achieved by changing meta-atoms' dimensions and orientations.^[37] Importantly, the phase is directly related to the displacement and can thus be continuously modulated, independent of the incident angle and wavelength. Based on this diatomic metasurface, broadband vectorial holographic images have been demonstrated. Later on, this concept has been extended to multifreedom metasurfaces by the same group, which can tailor amplitude, phase, polarization, and frequency simultaneously.^[54] With an MIM architecture, full-color vectorial meta-holograms with both amplitude and phase modulation were experimentally realized in the visible, which significantly increases the information capability.

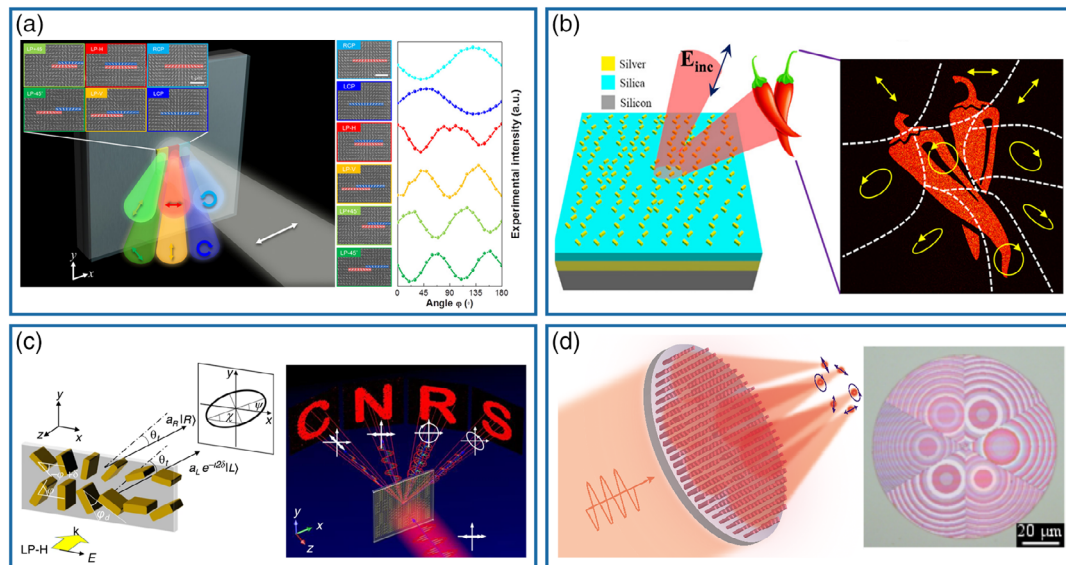


Figure 4. All-polarization converters based on metasurfaces. a) Left panel: illustrate of an Al GSP metasurface that produces arbitrary SOPs with a LP light source. Right panel: measured diffraction intensity of six polarizations as a function of the QWP's orientation. The inset shows the SEM images of the fabricated samples with each supercell highlighted. b) schematic of the diatomic metasurface for the vectorial holographic display under a LP light. The unit cell consists of two orthogonal plasmonic nanorods. c) Left panel: working principle of full-polarization generation by merging two output CP beams with arbitrary phases and amplitude ratios under an LP incident beam. Right panel: illustration of the polarization-encoded metahologram with images reconstructed in different directions. d) Left panel: schematic of the strategy of arbitrary polarization generation and manipulation with a metapolarizer, which converts an x -polarized beam into six beams possessing arbitrary polarization states and wavefronts. Right panel: the optical image of the fabricated metalens for all-polarization generation and focusing. a) Reproduced with permission.^[52] Copyright 2017, ACS. b) Reproduced with permission.^[53] Copyright 2018, ACS. c) Reproduced under the terms of Creative Commons Attribution (CC BY) license.^[57] Copyright 2020, The Authors, Published by Springer Nature. d) Reproduced with permission.^[58] Copyright 2020, Wiley-VCH.

Despite the great achievements in all-polarization generation with GSP metasurfaces, they are limited to reflection operation, whereas the diatomic metasurfaces only work under a specific incident angle,^[53,54] which restricts the range of potential applications. On the other hand, the efficiencies are intrinsically limited. For the PB-phase-based versatile polarization generator, the upper bound of the efficiency for a certain SOP produced in one direction is lower than 50% because of the twin beams.^[52] Regarding diatomic metasurfaces, the increased distance between two meta-atoms would reduce the efficiency.^[53] In this case, dielectric-metasurface all polarization converters could overcome the aforementioned constraints and be the ideal candidates for practical applications.^[56–58] Very recently, Song et al. demonstrated a full-polarization-reconstructed metasurface composed of GaN nanopillars to produce arbitrary SOPs from a LP incident light.^[57] The metasurface consists of two PB-phase gradient supercells, where the bottom meta-atoms are disposed in a counterclockwise-rotated line to deflect the LCP light to right with an angle of θ_b , and the top meta-atoms are arranged in a clockwise rotated top line to deflect the RCP light to the same angle of θ_t upon excitation with an x -polarized wave, as displayed in the left panel of Figure 4c. By engineering the orientations of both the bottom and top supercells with the angles of φ and $-\varphi + \delta$ respectively, a phase difference of -2δ is introduced between the LCP and RCP light, which is responsible for reconstructing arbitrary SOPs. At the same time, the amplitude ratio between LCP and RCP lights can be further controlled by adjusting the dimensions of dielectric meta-atoms. Therefore, arbitrary

SOPs can be obtained to cover the entire Poincaré sphere. With this concept, a polarization-encoded metahologram has been successfully demonstrated at $\lambda = 600$ nm. However, the maximum absolute efficiency of the holograms is only 25.4%, which is mainly ascribed to the unwanted ghost images generated by the periodicity of the supercells. To produce a specific polarization state with a certain phase, two supercells are needed to assemble the RCP and LCP beams, thereby resulting in subpixel arrangement and the corresponding grating effect.

To decrease the pixel size for each polarization state, a novel and versatile strategy that allows to efficiently produce arbitrary SOPs with controllable wavefronts from a LP incident beam has been proposed and demonstrated based on dielectric metasurfaces (Figure 4d).^[58] Different from the previous demonstrations based on PB metasurfaces, Ding et al. implemented this design using Si meta-atoms working as nanowaveplates with engineered phase responses. Specifically, independent and full control over both the polarization and phase (i.e., 2π phase range) of the transmitted beam with high efficiencies was realized at the design wavelength of $\lambda_d = 850$ nm by engineering the meta-atoms. Therefore, each meta-atom mimics the combined functionalities of a polarization converter and a phase modulator in a truly compact manner. With the designed nanowaveplates, six spatially separated transmitted beams possessing distinct and well-defined SOPs as well as specific wavefronts have been simultaneously generated from a LP light by segmenting six subarrays composed of amorphous Si meta-atoms in a circular configuration. In this design, the created six beams carrying different

SOPs are well separated in space, so the cross-talk between them is greatly suppressed, validated by the lower two-norm error ($\approx 6\%$) between the measured and predicted Stokes parameters at $\lambda_d = 850$ nm. In principle, more SOPs can be accordingly designed by dividing the metadvice into more sectors. However, the increased number of sectors and SOPs will result in more crosstalk and inhomogeneous output. Remarkably, the measured efficiency of the implemented polarization-resolved metalens is above 50% in the wavelength range from 800 to 1000 nm and the measured vectorial hologram efficiencies are $\approx 51\%$ for linear polarizations at $\lambda_d = 850$ nm. To increase the hologram efficiency, off-axis design and finer phase step could be used to decrease the unwanted zero order. In addition, single-crystalline Si with lower loss could be used to replace amorphous Si.

4. Metasurface-Based Polarimeters

4.1. Metasurface-Based Polarimeters for Polarization Detection

Polarimeters, which can detect and determine the SOP of light, are important in many realistic applications, ranging from remote sensing, polarization light imaging, ellipsometry, to medical diagnostics. In spite of all scientific potential, polarimetry is very hard to demonstrate as polarization is uncorrected with other channels of light, such as intensity and frequency. Typically, conventional methods utilize multiple measurements to obtain the Stokes parameters that fully determine the SOP. In this way, a complicated optical setup with a set of polarization elements arranged in front of a detector is needed, resulting in a complicated and high-cost setup. On other hand, the excellent capability of controlling the polarization state advances the progress of metasurface-based polarimeters,^[59–69] which can overcome bulky and expensive architectures and thus result in further miniaturization and potential integration with photonic systems. In early approaches, PB-phase metasurfaces have been used to determine the degree of circular polarization based on the spin-selective phase modulation.^[60,61] Specifically, the scattering intensity ratio between the RCP and LCP beams was utilized to determine the handedness and ellipticity of the light. But this method cannot retrieve all information on the incident polarization due to the limited channels (e.g., only two channels are included).

To completely detect and characterize the SOP of light, at least four uncorrected channels are needed.^[59,62–64] Recently, Pors et al. experimentally realized an MIM metagrating to simultaneously determine all polarization states.^[62] As shown in **Figure 5a**, three interleaved metasurfaces constitute the metagratings, in which each works independently as a polarization beam splitter for one of the three polarization bases with a particular periodicity. Upon excitation with a polarized incident beam with an unknown SOP, the metagrating creates six diffraction spots, through which Stokes parameters can be calculated, allowing for quick and accurate polarization detection. At the design wavelength of 800 nm, the obtained diffraction contrasts can replicate well the Poincaré sphere, as shown in the right panel of **Figure 5a**. In addition, the two-norm error between Stokes parameters and retrieved diffraction contrasts are as small as ≈ 0.1 . This approach is attractive because it shows a simple, fast but efficient way to measure the unknown SOP of any polarized light. Following this concept, Ding et al. demonstrated

self-calibrating segmented GSP metasurfaces with center-symmetrical configuration for spectropolarimeters that is capable of measuring the SOP and spectrum of incoming light beam simultaneously.^[65] In 2018, Wu et al. demonstrated a reflective integrated polarimeter that uses Al to construct PB metasurfaces to determine the Stokes parameters in the visible range.^[66]

However, reflective metasurfaces are not compatible with realistic applications. To address this issue, metasurface-based polarimeters consisting of all-dielectric birefringent meta-atoms have been used.^[67–69] Here, we would like to highlight a Si metapolarimeter array for Stokes parameters reconstruction from Faraon and coworkers.^[68] As shown in **Figure 5b**, the polarimeter focuses incident light into six spots on the detector. Thus, the intensities I_x , I_y , I_a , I_b , I_r , and I_l can be obtained by integrating the related pixel areas, which can be further used to retrieve the Stokes parameters. The right panel of **Figure 5b** shows the experimental results of the fabricated metasurface polarimeter, where intensity distributions of six characteristic spots change according to the incident SOPs. After averaging over about 120 superpixels, the Stokes parameters were obtained and found to be consistent with predicted values. In addition, the measured transmission efficiency is within the range of 60%–65%. Based on this platform, a metasurface mask for imaging a complicated polarization object has been created, which is promising for polarization cameras. Similarly, Yang et al. realized arrays of metalenses that allow for the determination of the polarization profile of an optical beam at a wavelength of 1550 nm.^[69] Furthermore, they extended this concept and demonstrated a compact Hartmann–Shack array shown in **Figure 5c**. By analyzing the amplitudes of focal spots, this metadvice can detect both polarization states and phase-gradient profiles. For the wavefront profiling, the measurement agrees well with the theoretical value and the relative error is around $\approx 1.05\%$ when the incident angle is less than 5° , superior to the usual Hartmann–Shack wavefront sensor.

4.2. Metasurface-Based Polarimeters for Polarization Imaging

In addition to polarimetry, optical metasurfaces can be implemented to realize direct polarization imaging combined with conventional optical components. In 2016, Capasso and coworkers used a planar metalens for chiral imaging based on interleaved titanium dioxide (TiO_2) meta-atoms with PB-phase modulation.^[70] In the metalens, each set of interleaved meta-atoms generates an off-axis focal spot on the same plane for the RCP and LCP lights. In 2019, they further extended this concept and successfully demonstrated a full-Stokes polarization camera with a compact footprint.^[71] As shown in **Figure 5d**, a TiO_2 metasurface-based matrix grating that enables parallel polarization analysis is integrated with an aspheric lens to image four diffraction orders on an imaging sensor. With one single shot, four images are formed, which could show different aspects of the polarization and give a full snapshot of polarization state at each pixel. It should be noted that this single-shot polarization camera does not require any moving parts or conventional polarization optics. In this way, it could find important applications in machine vision, remote sensing, and other related areas.

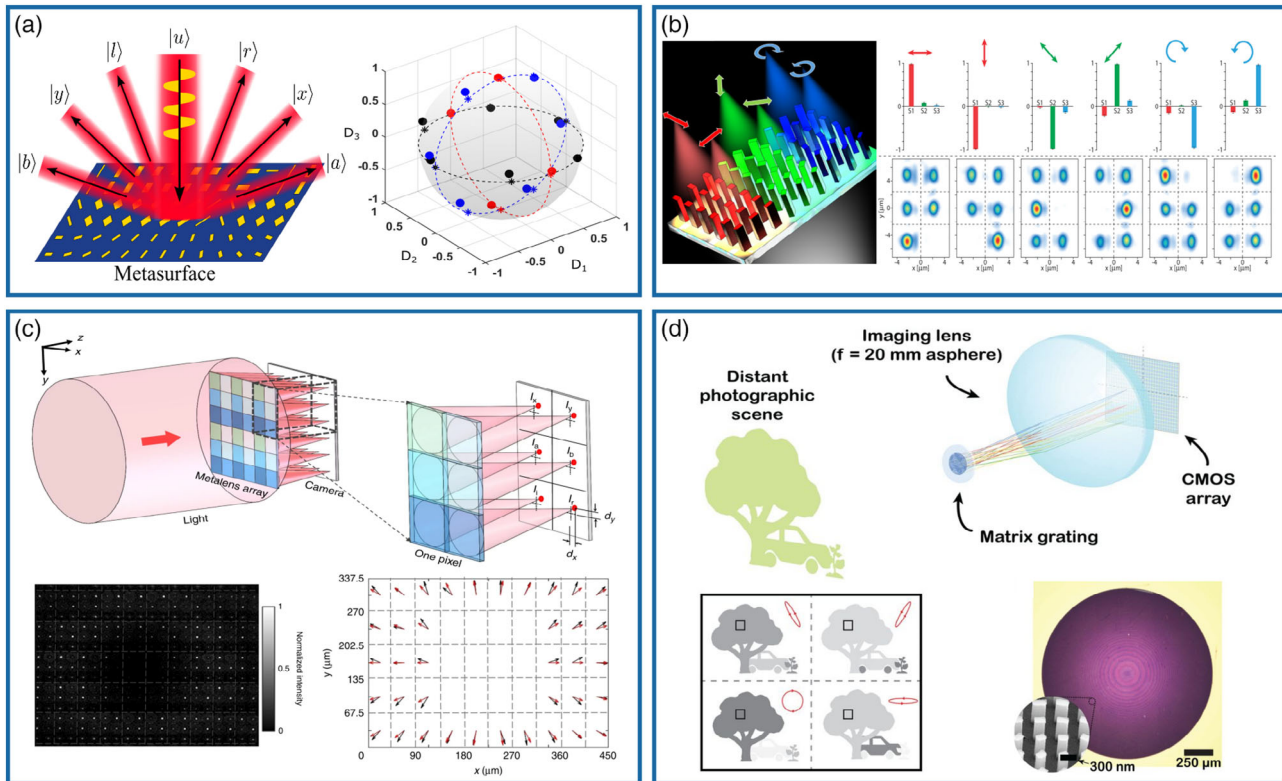


Figure 5. Metasurface-based polarimeters. a) Left panel: illustration of a metagrating polarimeter. Right panel: measured (filled circles) and predicted (asterisks) Stokes parameters on Poincaré sphere at $\lambda = 800$ nm. b) Left panel: schematic of a metasurface superpixel that focuses six different SOPs to separated spots. Right panel: measured Stokes parameters and the corresponding intensity distributions for a sample superpixel with different input polarizations. c) Top panel: schematic of a Si metasurface-based Hartmann–Shack sensor for SOP and phase profile characterization. Bottom left panel: focal spot images for a radially polarized beam. Bottom right panel: polarization profiles for the radially polarized beam, where the black and red arrows represent the measured and calculated local polarization vectors, respectively. d) Top panel: schematic of a compact full-Stokes polarization camera based on the TiO_2 matrix grating. Bottom left panel: optical and SEM images of the fabricated metasurface grating. Bottom right panel: polarization-resolved images. a) Reproduced under the terms of Creative Commons Attribution (CC BY) license.^[62] Copyright 2015, The Authors, Published by Optical Society of America (OSA). b) Reproduced with permission.^[68] Copyright 2018, ACS. c) Reproduced under the terms of Creative Commons Attribution (CC BY) license.^[69] Copyright 2018, The Authors, Published by Springer Nature. d) Reproduced with permission.^[71] Copyright 2019, the American Association for the Advancement of Science (AAAS).

5. Polarization-Multiplexed Metadevices

As mentioned in the previous sections, metasurfaces exhibit the unprecedented capability of manipulating the SOP with a subwavelength spatial resolution, which has boosted development activities in polarization conversion and detection. Meanwhile, polarization has been widely used to multiplex the functionalities of metasurfaces, resulting in increased capacity for information processing. In this section, we try to review some polarization-multiplexed metadevices in the optical regime.

5.1. Linear-Polarization-Multiplexed Metadevices

5.1.1. Linear-Polarization-Multiplexed Plasmonic Metadevices Based on Anisotropic Meta-Atoms

As shown in Equation (3), anisotropic meta-atoms are sensitive to the incident linear polarization states and have distinct responses along the two main axes. Therefore, isotropic metasurfaces can

be used to construct metadevices with different functionalities encoded with two orthogonal linear polarization states. For example, Pors et al. utilized GSP reflective metasurfaces, composed of periodic metallic nanobricks, to modulate the reflection phases of orthogonal linear polarizations independently, as shown in **Figure 6a**.^[72] By properly engineering the bricks' dimensions along two directions, the incident LP beams experience opposite phase gradients for the x - and y -polarization, thereby anomalously deflecting the reflected beams into ± 1 diffraction orders, respectively (right panel of Figure 6a). However, the measured efficiency is $\approx 50\%$, much lower compared with the theoretical value of $\approx 80\%$. The discrepancy is associated with the errors in fabrication and uncertainties in the optical constants of deposited materials. Later on, high-order GSP resonances^[73,74] and dual-wavelength meta-atoms^[75] were used to implement polarization beam-splitters that possess considerable polarization contrast and robust angular independence. In addition to polarization beam splitting, anisotropic GSP metasurfaces could efficiently launch surface plasmon polaritons (SPPs) in

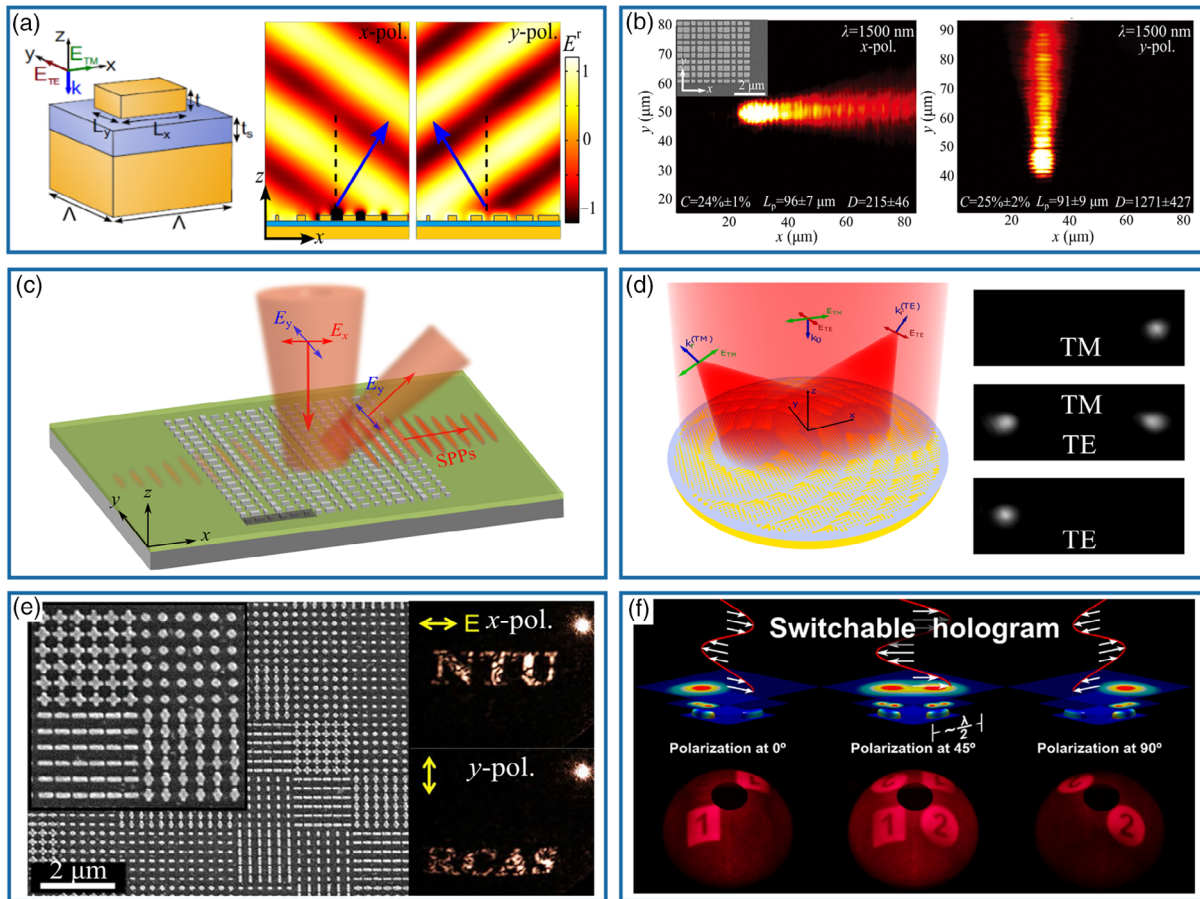


Figure 6. Linear-polarization-multiplexed plasmonic metadevices based on anisotropic meta-atoms. a) Left panel: schematic of a GSP unit cell for polarization-sensitive beam-steering. Right panel: simulated reflected electric fields for x - and y -polarized light at normal incidence. b) Optical characterization of a polarization-controlled directional SPP coupler at $\lambda = 1500$ nm, with the coupling efficiency C , propagation length L_p , and directivity D indicated. The inset in the left panel shows the SEM image of the fabricated sample. c) Schematic of a bifunctional visible GSP metasurfaces that achieves polarization-controlled unidirectional SPP excitation and beam-steering at normal incidence. d) Left panel: schematic of a multifunctional metasurface that enables focusing and polarization beam-splitting with a high efficiency and a high extinction ratio. e) Experimental demonstration of an MIM metasurface for linear-polarization-multiplexed holograms. f) Simulations and experimental results for reconstructing two independent holograms when the electric field is at 0° , 45° , and 90° , respectively. a) Reproduced under the terms of Creative Commons Attribution (CC BY) license.^[72] Copyright 2013, The Authors, Published by Springer Nature. b) Reproduced under the terms of Creative Commons Attribution (CC BY) license.^[76] Copyright 2014, The Authors, Published by Springer Nature. c) Reproduced under the terms of Creative Commons Attribution (CC BY) license.^[78] Copyright 2018, The Authors, Published by Springer Nature. d) Reproduced with permission.^[79] Copyright 2018, ACS. e) Reproduced with permission.^[80] Copyright 2013, ACS. f) Reproduced with permission.^[81] Copyright 2013, ACS.

orthogonal directions when the in-plane phase gradient is designed to match the wavevector of SPPs.^[76,77] Figure 6b shows an unidirectional polarization-controlled metacoupler at telecom wavelengths, which can couple normally incident LP light (i.e., x - or y -polarization) into SPPs propagating along orthogonal directions.^[76] The sample is made up of 6×6 MIM supercells, whose phase gradients are carefully designed to match the wavevectors of SPPs. Experimental measurements indicate that the fabricated sample can achieve the desired bidirectional SPP coupling with the coupling efficiencies of $\approx 25\%$ and the directivities exceeding 100. Recently, Ding and coworkers extended this concept to the visible wavelength and demonstrated a bifunctional MIM meta-device that can realize different functionalities (e.g., SPP coupling and beam steering) simultaneously upon excitation with

two LP beams at normal incidence.^[78] The device was constructed by anisotropic MIM meta-atoms and works properly in a broad wavelength range from 580 to 700 nm (see Figure 6c).

Apart from linear phase gradients, polarization-encoded parabolic phase profiles for planar metalens can be achieved with GSP meta-atoms.^[42,79] Boroviks et al. demonstrated a multifunctional metasurface that enables focusing and polarization splitting simultaneously with a high efficiency and wide operation bandwidth.^[79] Similar to the studies by Pors et al. and Ding et al.,^[76,78] the design relies on anisotropic MIM meta-atoms that host different GSP modes and thus supply linear-polarization-sensitive phase gradients for reflected fields, as shown in Figure 6d. Specifically, the MIM structure is composed of Au nanobricks with different lateral dimensions arranged in a

periodic array with a subwavelength periodicity, a silicon dioxide spacer, and a bottom thick Au substrate. The fabricated device has an efficiency of $\approx 65\%$ and a polarization extinction ratio up to ≈ 30 dB in a broadband spectrum from 750 to 950 nm. In addition to parabolic phase profiles, more complicated phase distributions can be achieved for individual linear polarization, e.g., polarization-encoded metaholograms.^[80,81] As a result, distinct images can be selectively reconstructed by switching the orientation of the incident linear polarization. For example, Chen et al. utilized an MIM metasurface with cross-shaped topmost Au nanorods to realize a four-level phase-modulated metahologram that can reconstruct dual images with respect to the incident linear polarization states, as shown in Figure 6e.^[80] In the design, the electric dipole resonances of a single nanorod along two directions can be selectively excited by a LP incident beam with proper polarization states. In the experiment, two reconstructed images can be clearly observed under two orthogonal LP light beams with a measured efficiency of 18%. Capitalizing on this idea, Montelongo et al. realized polarization-multiplexed holography in visible with selective radiation from plasmonic nanoantennas (Figure 6f).^[81] They fabricated a switchable hologram capable of reconstructing images with a high resolution over a wide field of view, which arranges two sets of coplane nanoantennas without producing interference in far-field, resulting in the superposition of two independent polarizations in a subwavelength distance without crosstalk.

5.1.2. Linear-Polarization-Multiplexed Dielectric Metadevices Based on Anisotropic Meta-Atoms

In addition to plasmonic metasurfaces, linear-polarization-multiplexed metasurfaces can be implemented with anisotropic all-dielectric meta-atoms. Gao et al. proposed and demonstrated a highly efficient bifunctional dielectric metasurface, whose building block capitalizes on anisotropic nanoposts made up of hydrogenated amorphous Si, as shown in Figure 7a.^[82] Therefore, visible polarization-encoded focusing and anomalous beam-steering were implemented. By tailoring the unit cell's periodicity, the angle of beam deflection and distance of focusing can be effectively tuned. In the experiment, the fabricated sample exhibits a bright-line focus for the normally incident transverse-magnetic-polarized light from 600 to 715 nm, whereas the normal transverse-electric incidence is deflected to the desired diffraction order. Schonbrun et al. demonstrated two metalenses composed of Si nanowires with elliptical cross sections, which enable dynamically reconfigured imaging when the incident light is switched between different linear polarization states.^[83] For each Si nanowire, polarization-sensitive focusing functionalities are encoded. As shown in Figure 7b, the first nanowire lens possesses different focal lengths for horizontal and vertical polarization states, demonstrating a dynamic zoom imaging system. The second nanowire lens has different optical axes for two linear polarization states, indicating stereoscopic imaging capability. Yang et al. demonstrated reflective-type polarization-sensitive color printing using TiO₂ elliptic meta-atoms, where anisotropic resonances along two axes are supported to provide different dispersive amplitude modulation for orthogonal LP polarizations (Figure 7c).^[84] In particular, by varying periodicities of the

meta-atoms along the x - and y -directions, Fano resonance is available and can be used to realize dual colors with a very sharp contrast under two orthogonal linear polarizations. Figure 7d shows a good example on how to utilize dielectric metasurfaces to manipulate phase and polarization, completely, and independently, as well as to realize polarization-multiplexed functionalities.^[37] In the design, each elliptical Si meta-atom can be regarded as a truncated waveguide, whose anisotropic cross section results in different effective mode indices with the polarization states along the major and minor axes. Therefore, each meta-atom imposes a polarization-dependent phase distribution for transmitted fields, leading to complete control over both the phase and polarization by changing the lateral dimensions (e.g., major axis and minor axis) of the elliptical Si posts. As a result, polarization-encoded dual images can be realized in a single subwavelength element with a high transmission efficiency of around $\approx 97\%$ and greatly suppressed unwanted diffraction orders.

5.2. Circular-Polarization-Multiplexed Metadevices

5.2.1. Spin-Coupled Metadevices with Merged Meta-Atoms

Similar to the linear polarization, the circular polarization or spin is frequently utilized to realize multifunctional metadevices capitalizing on PB phase.^[2–12,85] As the PB phase has locked and opposite signs for two spins, the functionalities for RCP and LCP beams are typically mirrored, such as beam-steering into opposite diffraction orders,^[14,86] SPP coupling to opposite directions,^[87–89] and optical vortexes carrying opposite topological charges.^[64,90–92] For example, Khorasaninejad and Crozier demonstrated a planar dielectric chirality-distinguishing beam-splitter consisting of amorphous Si meta-atoms on a transparent substrate.^[86] As shown in Figure 8a, the fabricated beam-splitter deflects LCP and RCP beams into different directions. Recently, Hasman and coworkers demonstrated photonic spin-controlled multifunctional metadevices by combining the PB phase with the shared-aperture concept,^[64,90,91] among which spin-controlled multiple wavefronts such as optical vortexes with different orbital angular momentum (OAM) were implemented at $\lambda = 780$ nm (Figure 8b).^[64] In addition to the shared-aperture concept, random patterns have also been combined with PB phase to superpose metasurface patterns in a 2D manner, which can extend the information capability.^[90] By manipulating the local orientations of the mixed random meta-atoms in different groups, multiple wavefronts with distinct functionalities can be generated, where each group corresponds to a particular phase profile (Figure 8c).

Nevertheless, the aforementioned spin-multiplexed metadevices have intrinsically locked functionalities for input beams with two different spins, which limits the practical applications. To realize multiple distinct functionalities for CP beams, one common approach is to merging or superposing several PB metasurfaces together into one single device, where each metasurface exhibits a certain functionality corresponding to the incident spin.^[92–95] In 2015, Huang et al. used PB metasurfaces to record multiple holograms in spin-multiplexed channels (Figure 8d).^[95] Due to the wideband nature of PB metasurfaces, holography covering the spectrum range of 633–1000 nm was demonstrated. However, the measured efficiency was quite low (for instance,

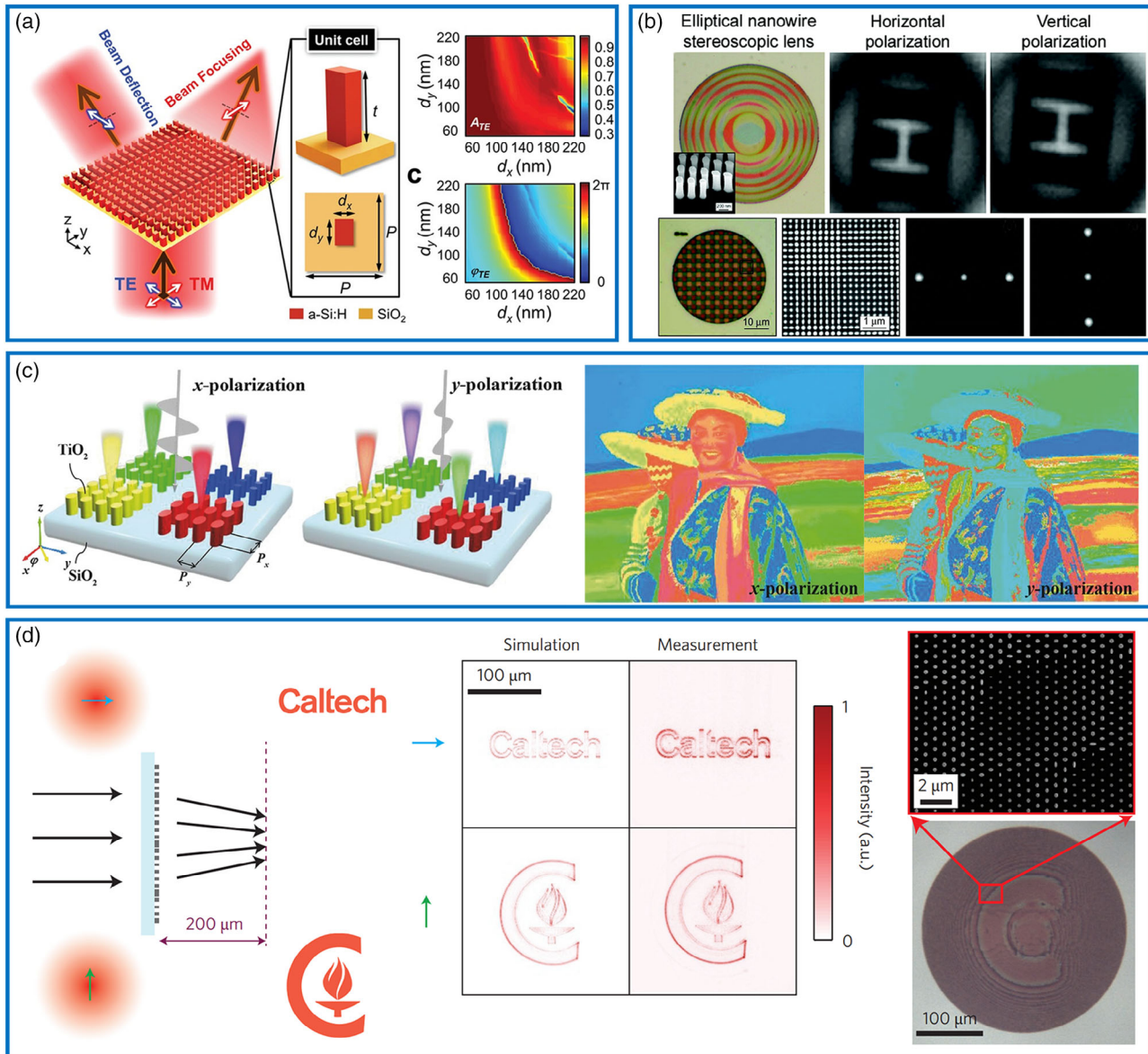


Figure 7. Linear-polarization-multiplexed dielectric metadevices based on anisotropic meta-atoms. a) Schematic of a linear-polarization-switchable bifunctional metasurface for beam-steering and focusing in visible. b) Bright field microscope and SEM images of the 2D elliptical nanowire gratings which can take a different focal length or has a different optical axis for each linear polarization state. c) Schematic of a TiO₂ metasurface for polarization-sensitive structural color in reflection. d) Left panel: schematic of a polarization-encoded phase hologram that generates different patterns for x- and y-polarized light. Middle panel: simulated and measured intensity profiles. Right panel: optical (bottom) and SEM (top) images of the devices. a) Reproduced with permission.^[82] Copyright 2019, Wiley-VCH. b) Reproduced with permission.^[83] Copyright 2011, ACS. c) Reproduced with permission.^[84] Copyright 2018, Wiley-VCH. d) Reproduced with permission.^[37] Copyright 2015, Springer Nature.

4.5% at 810 nm). Figure 8e shows a bifunctional optical metasurface that produces a vortex beam or a hologram image, depending on the incident spin.^[96] In this design, the authors first designed two individual PB metasurfaces based on metal-bar structures with specific orientations and locations to impart the PB phase, which can produce either a vortex beam or a hologram when illuminated with CP light. Then they merged these two PB metasurfaces to make a single metadevice in which all meta-atoms do not touch each other. The fabricated metadevice exhibits excellent bifunctional performance when the incident

spin is altered. But the working efficiency is rather limited, which is only $\approx 9\%$. To increase the efficiency, GSP PB metasurfaces that can produce spin-multiplexed broadband holograms have been demonstrated by Wen et al.^[97] As shown in Figure 8f, two different holograms corresponding to LCP and RCP incident lights are first calculated by the Gerchberg–Saxton algorithm, and then encoded in the MIM metasurfaces with the “merging” concept. By finely tuning the orientation of the Ag nanorods, uniform reflection amplitude and 16-level phase profiles covering 2π phase range could be obtained. Therefore, the reconstructed

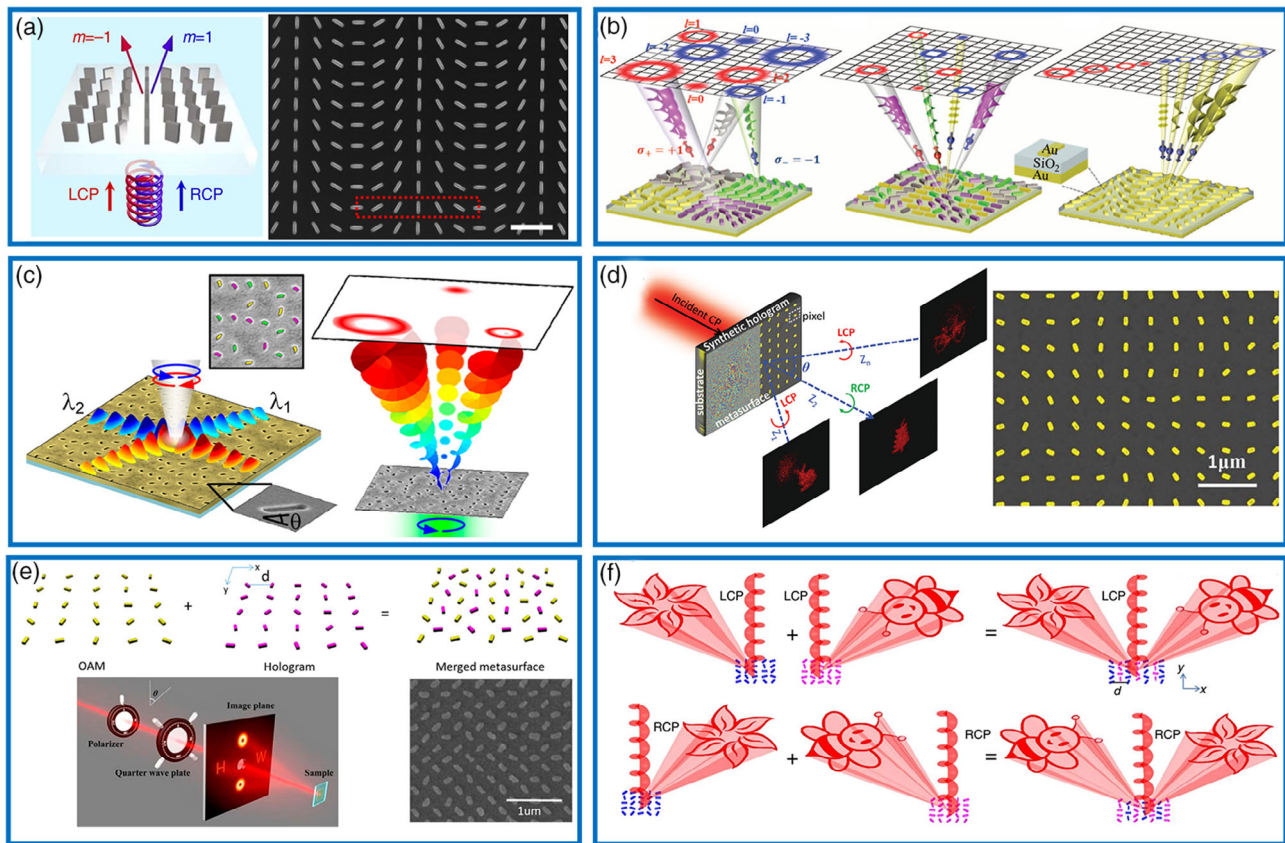


Figure 8. Spin-coupled metadevices with merged meta-atoms. a) Left panel: schematic diagram of a spin-distinguishing beam splitter, which redirects the impinging light based on its spin. Right panel: top-view SEM image of a fabricated sample composed of Si nanofins. b) Schematic far-field intensity distribution of wavefronts containing OAMs with positive (red) and negative (blue) spins generated from segmented, interleaved, and harmonic response PB phase GSP metasurfaces (the unit cell is shown in inset). c) Left panel: schematic of directional SPP channels opened by a disordered metasurface. Right panel: illustration of spin-controlled wavefront shaping with different OAMs generated by a disordered gradient metasurface. d) Left panel: schematic of a PB metasurface that reconstructs different images in different polarization channels. Right panel: SEM of a fabricated sample. e) Schematic of a “merging” concept for the realization of a multifunctional metasurface that enable spin-selective functionalities, i.e., a holographic image or a vortex beam. f) Schematic of a metasurface that reconstructs multiple holographic images when illuminated by CP beams with different spins. a) Reproduced under the terms of Creative Commons Attribution (CC BY) license.^[86] Copyright 2014, The Authors, Published by Springer Nature. b) Reproduced with permission.^[64] Copyright 2016, AAAS. c) Reproduced with permission.^[90] Copyright 2015, ACS. d) Reproduced with permission.^[95] Copyright 2015, Wiley-VCH. e) Reproduced with permission.^[96] Copyright 2017, ACS. f) Reproduced under the terms of Creative Commons Attribution (CC BY) license.^[97] Copyright 2015, The Authors, Published by Springer Nature.

holograms (e.g., the spin-dependent flower or bee) have a measured efficiency up to 59.2% at 860 nm, whereas the good performance is maintained from 475 to 1100 nm with the efficiency >40%. As a final comment, it is worth noting that although this “merging” strategy is physically straightforward and can make the distinct functionalities for two different spins, the realized devices exhibit limited working efficiencies and suffer from intrinsic crosstalk.^[92–97]

5.2.2. Spin-Decoupled Metadevices

Very recently, the spin-locked limitation of PB metasurfaces has been released by combining the orientation-determined PB phase and the dimension-dependent propagation or resonance phase together, providing a versatile approach toward the demonstration of spin-decoupled multiple functionalities in a single

metadvice for two CP beams.^[37,98] As such, numerous spin-decoupled multifunctional metadevices have been implemented using this approach, including spin-encoded holograms,^[98,99] spin-to-orbital momentum converters,^[100] spin-decoupled multifocal lenses,^[101–103] and spin-decoupled polarization conversion and wavefront shaping.^[104–106] In 2017, Capasso and coworkers invented this basic approach that combines PB and propagating phases together to manipulate the phase profiles of any two orthogonal polarization states. In the experiment, they demonstrated chiral holograms in the transmission-mode using TiO₂ metasurfaces, which can produce uncorrelated holographic images with high efficiencies under CP excitations at $\lambda = 532$ nm (Figure 9a).^[98] In 2019, Overvig et al. realized a Si metasurface allowing for both phase and amplitude control, through which far-field holography and monochromatic gray-scale nanoprinting have been demonstrated (Figure 9b).^[107]

Specifically, both the propagation phase and PB phase were modulated by varying the sizes of Si meta-atoms, thereby determining the degree of birefringence and rotation angles. As a result, the incident CP light can be converted into any polarization state. By applying a polarization filter to select the cross-polarized components, its amplitude can be continuously varied, whereas the related phase is represented by the sum of the PB phase and the propagation phase. In addition to the intensity and phase design, the so-called full Fourier components control method has been recently proposed and demonstrated with Si metasurfaces,^[108] where the multiple channels with no or weak noises were designed in Fourier space, thereby resulting in the development in multidimensional polarization-multiplexed metadevices.^[109]

In spite of the aforementioned spin-decoupled metasurfaces for transmitted fields, spin-decoupled optical metadevices that can control both propagating waves and surface waves are still largely unexplored. In 2020, Meng et al. demonstrated spin-controlled unidirectional SPP excitation and beam-steering in the near-infrared range using GSP meta-atoms that function as nano-HWPs, as shown in the top panel of Figure 9c.^[110] In the design, four GSP nano-HWPs were designed to impart two distinct spin-sensitive linear-phase gradients along the x -direction due to the combined contributions from PB phase and resonance phase (bottom panel of Figure 9c). Under RCP excitation, the phase gradient is matched to the wavevector of SPPs supported on the substrate at normal incidence. Once

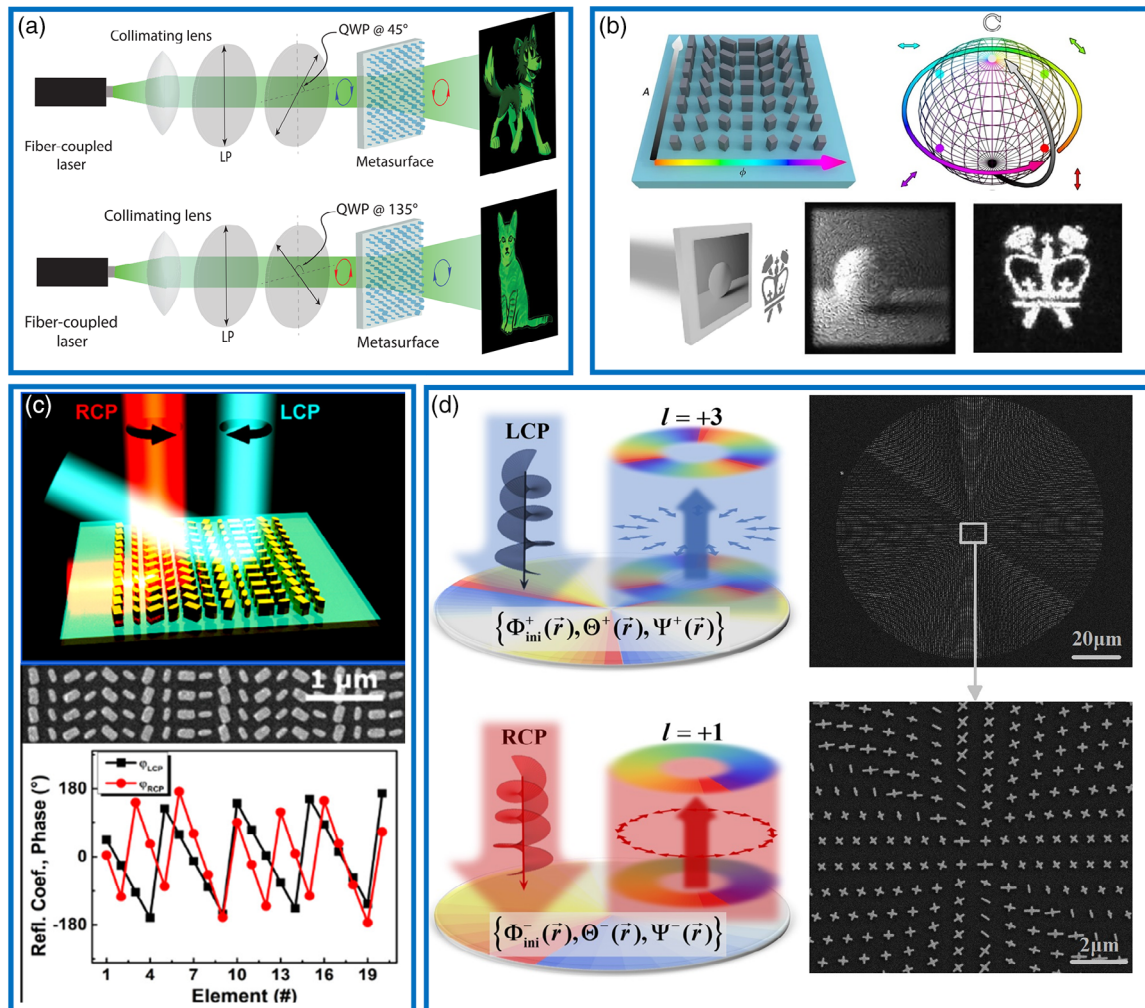


Figure 9. Spin-decoupled metadevices. a) Schematic of chiral holograms based on a single TiO_2 metasurface that encodes two independent phase profiles for LCP and RCP beams at $\lambda = 532$ nm. b) Top panel: schematic of the Si meta-atoms with varied geometries that provide the amplitude and phase control to convert LCP incident light to any other point on the Poincaré sphere with near-unity efficiency. Bottom panel: experimental reconstructions when focused onto the metasurface and object planes, respectively. c) Top panel: schematic of the spin-decoupled bifunctional GSP metasurface for unidirectional SPP excitation and beam-steering under RCP and LCP excitations at normal incidence, respectively. Middle panel: SEM image of the fabricated sample. Bottom panel: realized phase profiles of reflected fields under two spins at $\lambda = 850$ nm. d) Left panel: schematics of light scatterings at a metadevice exhibiting vortex wavefronts carrying different topological charges under illuminations of LCP and RCP incidences. Right panel: SEM images of the fabricated sample. a) Reproduced with permission.^[98] Copyright 2017, APS. b) Reproduced under the terms of Creative Commons Attribution (CC BY) license.^[107] Copyright 2019, The Authors, Published by Springer Nature. c) Reproduced with permission.^[110] Copyright 2020, ACS. d) Reproduced under the terms of Creative Commons Attribution (CC BY) license.^[49] Copyright 2020, The Authors, Published by De Gruyter.

the incident light is switched to LCP, the phase gradient is smaller than the wavelength of propagating wave in free space, therefore resulting in anomalous reflection. The fabricated sample features efficient (>22%) unidirectional SPP launching and high-efficiency (48% on average) beam-steering in a wideband spectrum range of 850–950 nm for RCP and LCP incident light, respectively. Very recently, Zhou and coworkers designed a general method to realize high-efficiency metadevices that produce complex vectorial optical fields with desired wavefronts and polarization distributions (Figure 9d).^[49] By combining two different mechanisms for phase control, e.g., resonance phase and PB phase, they designed and fabricated bifunctional metadevices for dual vortex vectorial beam generation with distinct topological charges and polarization distributions.

6. Conclusion

We have reviewed the basic principles and some representative emerging applications of polarization-encoded functional optical metasurfaces. Due to the limited content, there are still some other important aspects not included within this short Review, such as nonlinear metasurfaces.^[111–118] Meanwhile, considering numerous novel concepts and following-up successful fancy applications, this emerging research area of polarization-encoded metasurfaces is developing very quickly. On the basis of this notion, herein, we show our prospects on two promising directions:

6.1. Polarization-Encoded Tunable Metasurfaces

So far, most of the polarization-encoded metasurfaces can only achieve passive and static functionalities. Indeed, to meet the increased demand for information-processing speed and capacity, it is desired to achieve polarization-multiplexed tunable metasurfaces by integrating active/reconfigurable elements, such as phase-changing materials,^[119–123] 2D materials,^[124,125] transparent conducting oxides,^[126–128] liquid crystals,^[129–132] microelectromechanical systems,^[133,134] catalytic materials,^[135,136] and PIN diodes,^[137] which could extend the functionalities and thus the information capabilities. For example, Luo and coworkers has successfully demonstrated multistate tunable phase-change metadevices, which allows to code information by combining the incident spins and multiple states.^[138]

6.2. Polarization-Encoded Quantum Metasurfaces

In addition to classical light, metasurfaces possess the capability of controlling nonclassical optical fields even at the single-photon level. For example, metasurface-enabled photon sources can produce polarized single-photon emission with a greatly enhanced emission rate.^[139–147] Due to the capability of polarization multiplexing, metasurfaces can replace the conventional bulky polarization optics and impose quantum entanglement or interference with the remotely generated single photons.^[148–150] As an emerging area of research, quantum metasurfaces could serve as a versatile platform for quantum nanophotonics, which may advance our understanding of light–matter interaction at the single-photon level, realize novel single-photon/

entangled-photon sources, and conduct high-dimensional quantum entanglement.^[151,152]

Acknowledgements

F.D. and S.T. contributed equally to this work. This work was funded by the University of Southern Denmark (SDU2020 funding), and Villum Fonden (award in Technical and Natural Sciences 2019, grant nos. 00022988 and 37372). S.T. acknowledges the support from the National Natural Science Foundation of China (grant no. 11604167), and Zhejiang Province Natural Science Foundation of China (grant no. LY19A040004).

Conflict of Interest

The authors declare no conflict of interest.

Keywords

metasurfaces, polarimeters, polarization converters, polarization-multiplexed devices

Received: December 5, 2020

Revised: February 18, 2021

Published online:

- [1] F. L. Pedrotti, L. S. Pedrotti, in *Introduction to Optics*, Prentice Hall, Upper Saddle River, NJ **1993**, pp. P333–P371.
- [2] A. V. Kildishev, A. Boltasseva, V. M. Shalaev, *Science* **2013**, *339*, 1232009.
- [3] N. Yu, F. Capasso, *Nat. Mater.* **2014**, *13*, 139.
- [4] H. Chen, Z. Liu, S. Chen, J. Tian, *Adv. Mater.* **2015**, *27*, 5410.
- [5] H. Chen, A. J. Taylor, N. Yu, *Rep. Prog. Phys.* **2016**, *79*, 076401.
- [6] P. Genevet, F. Capasso, F. Aieta, M. Khorasaninejad, R. Devlin, *Optica* **2017**, *4*, 139.
- [7] H.-H. Hsiao, C. H. Chu, D. P. Tsai, *Small Methods* **2017**, *1*, 1600064.
- [8] F. Ding, A. Pors, S. I. Bozhevolnyi, *Rep. Prog. Phys.* **2018**, *81*, 026401.
- [9] Q. He, S. Sun, S. Xiao, L. Zhou, *Adv. Opt. Mater.* **2018**, *40*, 1800415.
- [10] S. Kamali, E. Arbabi, A. Arbabi, A. Faraon, *Nanophotonics* **2018**, *7*, 1041.
- [11] X. Luo, *Adv. Opt. Mater.* **2018**, *6*, 1701201.
- [12] S. Sun, Q. He, J. Hao, S. Xiao, L. Zhou, *Adv. Opt. Photonics* **2019**, *11*, 380.
- [13] X. Ding, F. Monticone, K. Zhang, L. Zhang, D. Gao, S. N. Burokur, A. de Lustrac, Q. Wu, C.-W. Qiu, A. Alù, *Adv. Mater.* **2015**, *27*, 1195.
- [14] W. Luo, S. Xiao, Q. He, S. Sun, L. Zhou, *Adv. Opt. Mater.* **2015**, *3*, 1102.
- [15] T. Cai, S. Tang, G. Wang, H. Xu, S. Sun, Q. He, L. Zhou, *Adv. Opt. Mater.* **2017**, *5*, 1600506.
- [16] Z. Jiang, L. Kang, T. Yue, H. Xu, Y. Yang, Z. Jin, C. Yu, W. Hong, D. Werner, C. W. Qiu, *Adv. Mater.* **2020**, *32*, 1903983.
- [17] N. K. Grady, J. E. Heyes, D. R. Chowdhury, Y. Zeng, M. T. Reiten, A. K. Azad, A. J. Taylor, D. A. Dalvit, H. T. Chen, *Science* **2013**, *340*, 1304.
- [18] L. Liu, X. Zhang, M. Kenney, X. Su, N. Xu, C. Ouyang, Y. Shi, J. Han, W. Zhang, S. Zhang, *Adv. Mater.* **2014**, *26*, 5031.
- [19] S. Liu, T. J. Cui, Q. Xu, D. Bao, L. Du, X. Wan, W. X. Tang, C. Ouyang, X. Y. Zhou, H. Yuan, H. F. Ma, W. X. Jiang, J. Han, W. Zhang, Q. Cheng, *Light Sci. Appl.* **2016**, *5*, e16076.
- [20] R. C. Jones, *J. Opt. Soc. Am.* **1941**, *31*, 488.
- [21] G. G. Stokes, *Trans. Cambr. Philos. Soc.* **1852**, *96*, 399.

- [22] A. Pors, M. G. Nielsen, G. D. Valle, M. Willatzen, O. Albrektsen, S. I. Bozhevolnyi, *Opt. Lett.* **2011**, *36*, 1626.
- [23] Y. Zhao, A. Alù, *Nano Lett.* **2013**, *13*, 1086.
- [24] A. Pors, S. I. Bozhevolnyi, *Opt. Express* **2013**, *21*, 2942.
- [25] Z. H. Jiang, L. Lin, D. Ma, S. Yun, D. H. Werner, Z. Liu, T. S. Mayer, *Sci. Rep.* **2014**, *4*, 7511.
- [26] D. Wang, Y. Gu, Y. Gong, C.-W. Qiu, M. Hong, *Opt. Express* **2015**, *23*, 11114.
- [27] J. T. Heiden, F. Ding, J. Linnet, Y. Yang, J. Beermann, S. I. Bozhevolnyi, *Adv. Opt. Mater.* **2019**, *7*, 1801414.
- [28] A. Pors, M. G. Nielsen, S. I. Bozhevolnyi, *Opt. Lett.* **2013**, *38*, 513.
- [29] S. C. Jiang, X. Xiong, Y. S. Hu, Y. H. Hu, G. B. Ma, R. W. Peng, C. Sun, M. Wang, *Phys. Rev. X* **2014**, *4*, 021026.
- [30] Y. Yang, W. Wang, P. Moitra, I. I. Kravchenko, D. P. Briggs, J. Valentine, *Nano Lett.* **2014**, *14*, 1394.
- [31] S. Kruk, B. Hopkins, I. I. Kravchenko, A. Miroshnichenko, D. N. Neshev, Y. S. Kivshar, *APL Photon.* **2016**, *1*, 030801.
- [32] F. Ding, Y. Yang, R. A. Deshpande, S. I. Bozhevolnyi, *Nanophotonics* **2018**, *7*, 1129.
- [33] I. Kuznetsov, A. E. Miroshnichenko, M. L. Brongersma, Y. S. Kivshar, B. Luk'yanchuk, *Science* **2016**, *354*, aag2472.
- [34] Y. Zhang, Z. Li, W. Liu, Z. Li, H. Cheng, S. Chen, J. Tian, *Adv. Opt. Mater.* **2019**, *7*, 1801273.
- [35] W. Liu, Z. Li, H. Cheng, S. Chen, *iScience* **2020**, *23*, 101868.
- [36] F. Ding, Z. Wang, S. He, V. M. Shalaev, A. V. Kildishev, *ACS Nano* **2015**, *9*, 4111.
- [37] A. Arbabi, Y. Horie, M. Bagheri, A. Faraon, *Nat. Nanotechnol.* **2015**, *10*, 937.
- [38] F. Ding, R. Deshpande, C. Meng, S. I. Bozhevolnyi, *Nanoscale* **2020**, *12*, 14106.
- [39] F. Ding, Y. Chen, S. I. Bozhevolnyi, *Photonics Res.* **2020**, *8*, 707.
- [40] D. Lin, P. Fan, E. Hasman, M. L. Brongersma, *Science* **2014**, *345*, 298.
- [41] M. Khorasaninejad, W. T. Chen, R. C. Devlin, J. Oh, A. Y. Zhu, F. Capasso, *Science* **2016**, *352*, 1190.
- [42] S. M. Wang, P. C. Wu, V.-C. Su, Y.-C. Lai, C. H. Chu, J.-W. Chen, S.-H. Lu, J. Chen, B. Xu, C.-H. Kuan, T. Li, S. Zhu, D. P. Tsai, *Nat. Commun.* **2017**, *8*, 187.
- [43] W. T. Chen, A. Y. Zhu, V. Sanjeev, M. Khorasaninejad, Z. Shi, E. Lee, F. Capasso, *Nat. Nanotechnol.* **2018**, *13*, 220.
- [44] J. Li, S. Chen, H. Yang, J. Li, P. Yu, H. Cheng, C. Gu, H.T. Chen, J. Tian, *Adv. Funct. Mater.* **2015**, *25*, 704.
- [45] F. Yue, D. Wen, J. Xin, B. D. Gerardot, J. Li, X. Chen, *ACS Photonics* **2016**, *3*, 1558.
- [46] Q. Ma, C. B. Shi, G. D. Bai, T. Y. Chen, A. Noor, T. J. Cui, *Adv. Opt. Mater.* **2017**, *5*, 1700548.
- [47] F. Ding, Y. Chen, Y. Yang, S. I. Bozhevolnyi, *Adv. Opt. Mater.* **2019**, *7*, 1900724.
- [48] F. Ding, Y. Chen, S. I. Bozhevolnyi, *Nanophotonics* **2020**, *9*, 371.
- [49] D. Wang, T. Liu, Y. Zhou, X. Zheng, S. Sun, Q. He, L. Zhou, *Nanophotonics* **2020**, 20200465.
- [50] N. Yu, F. Aieta, P. Genevet, M. A. Kats, Z. Gaburro, F. Capasso, *Nano Lett.* **2012**, *12*, 6328.
- [51] A. Shaltout, J. Liu, V. M. Shalaev, A. V. Kildishev, *Nano Lett.* **2014**, *14*, 4426.
- [52] P. C. Wu, W.-Y. Tsai, W. T. Chen, Y.-W. Huang, T.-Y. Chen, J.-W. Chen, C. Y. Liao, C. H. Chu, G. Sun, D. P. Tsai, *Nano Lett.* **2017**, *17*, 445.
- [53] Z.-L. Deng, J. Deng, X. Zhuang, S. Wang, K. Li, Y. Wang, Y. Chi, X. Ye, J. Xu, G. P. Wang, R. Zhao, X. Wang, Y. Cao, X. Cheng, G. Li, X. Li, *Nano Lett.* **2018**, *18*, 2885.
- [54] Z.-L. Deng, M. Jin, X. Ye, S. Wang, T. Shi, J. Deng, N. Mao, Y. Cao, B. Guan, A. Alù, G. Li, X. Li, *Adv. Funct. Mater.* **2020**, *30*, 2070131.
- [55] Y. Gao, X. Xiong, Z. Wang, F. Chen, R. Peng, M. Wang, *Phys. Rev. X* **2020**, *10*, 031035.
- [56] N. A. Rubin, A. Zaidi, M. Juhl, R. P. Li, J. P. B. Mueller, R. C. Devlin, K. Leósson, F. Capasso, *Opt. Express* **2018**, *26*, 21455.
- [57] Q. H. Song, A. Baroni, R. Sawant, P. Ni, V. Brandli, S. Chenot, S. Veziar, B. Damilano, P. de Mierry, S. Khadir, P. Ferrand, P. Genevet, *Nat. Commun.* **2020**, *11*, 2651.
- [58] F. Ding, B. Chang, Q. Wei, L. Huang, X. Guan, S. I. Bozhevolnyi, *Laser Photonics Rev.* **2020**, *14*, 2000116.
- [59] F. Ding, Y. Chen, S. I. Bozhevolnyi, *Appl. Sci.* **2018**, *8*, 594.
- [60] A. Shaltout, J. Liu, A. Kildishev, V. Shalaev, *Optica* **2015**, *2*, 860.
- [61] D. Wen, F. Yue, S. Kumar, Y. Ma, M. Chen, X. Ren, P. E. Kremer, B. D. Gerardot, M. R. Taghizadeh, G. S. Buller, X. Chen, *Opt. Express* **2015**, *23*, 10272.
- [62] A. Pors, M. G. Nielsen, S. I. Bozhevolnyi, *Optica* **2015**, *2*, 716.
- [63] J. P. B. Mueller, K. Leoson, F. Capasso, *Optica* **2016**, *3*, 42.
- [64] E. Maguid, I. Yulevich, D. Veksler, V. Kleiner, M. L. Brongersma, E. Hasman, *Science* **2016**, *352*, 1202.
- [65] F. Ding, A. Pors, Y. Chen, V. A. Zenin, S. I. Bozhevolnyi, *ACS Photonics* **2017**, *4*, 943.
- [66] P. C. Wu, J.-W. Chen, C.-W. Yin, Y.-C. Lai, T. L. Chung, C. Y. Liao, B. H. Chen, K.-W. Lee, C.-J. Chuang, C.-M. Wang, D. P. Tsai, *ACS Photonics* **2018**, *5*, 2568.
- [67] S. Wei, Z. Yang, M. Zhao, *Opt. Lett.* **2017**, *42*, 1580.
- [68] E. Arbabi, S. M. Kamali, A. Arbabi, A. Faraon, *ACS Photonics* **2018**, *5*, 3132.
- [69] Z. Yang, Z. Wang, Y. Wang, X. Feng, M. Zhao, Z. Wan, L. Zhu, J. Liu, Y. Huang, J. Xia, M. Wegener, *Nat. Commun.* **2018**, *9*, 4607.
- [70] M. Khorasaninejad, W. T. Chen, A. Y. Zhu, J. Oh, R. C. Devlin, D. Rousso, F. Capasso, *Nano Lett.* **2016**, *16*, 4595.
- [71] N. A. Rubin, G. D'Aversa, P. Chevalier, Z. Shi, W. T. Chen, F. Capasso, *Science* **2019**, *365*, eaax1839.
- [72] A. Pors, O. Albrektsen, I. P. Radko, S. I. Bozhevolnyi, *Sci. Rep.* **2013**, *3*, 2155.
- [73] R. A. Deshpande, A. Pors, S. I. Bozhevolnyi, *Opt. Express* **2017**, *25*, 12508.
- [74] R. A. Deshpande, F. Ding, S. Bozhevolnyi, *ACS Appl. Mater. Interfaces* **2020**, *12*, 1250.
- [75] S. Tang, F. Ding, T. Jiang, T. Cai, H. Xu, *Opt. Express* **2018**, *26*, 23760.
- [76] A. Pors, M. G. Nielsen, T. Bernardin, J. Weeber, S. I. Bozhevolnyi, *Light Sci. Appl.* **2014**, *3*, e197.
- [77] F. Ding, S. I. Bozhevolnyi, *IEEE J. Sel. Top. Quantum Electron.* **2019**, *25*, 1–.
- [78] F. Ding, R. Deshpande, S. I. Bozhevolnyi, *Light Sci. Appl.* **2018**, *7*, 17178.
- [79] S. Boroviks, R. A. Deshpande, N. A. Mortensen, S. I. Bozhevolnyi, *ACS Photonics* **2018**, *5*, 1648.
- [80] W. T. Chen, K. Yang, C. Wang, Y. Huang, G. Sun, I. Chiang, C. Y. Liao, W. Hsu, H. T. Lin, S. Sun, L. Zhou, A. Q. Liu, D. P. Tsai, *Nano Lett.* **2013**, *14*, 225.
- [81] Y. Montelongo, J. O. Tenorio-Pearl, W. I. Milne, T. D. Wilkinson, *Nano Lett.* **2013**, *14*, 294.
- [82] S. Gao, C. S. Park, S. S. Lee, D. Y. Choi, *Adv. Opt. Mater.* **2019**, *7*, 1801337.
- [83] E. Schonbrun, K. Seo, K. B. Crozier, *Nano Lett.* **2011**, *11*, 4299.
- [84] B. Yang, W. Liu, Z. Li, H. Cheng, S. Chen, J. Tian, *Adv. Opt. Mater.* **2018**, *6*, 1701009.
- [85] L. Huang, X. Chen, H. Mühlenbernd, H. Zhang, S. Chen, B. Bai, Q. Tan, G. Jin, K. Cheah, C. Qiu, J. Li, T. Zentgraf, S. Zhang, *Nat. Commun.* **2013**, *4*, 2808.
- [86] M. Khorasaninejad, K. B. Crozier, *Nat. Commun.* **2014**, *5*, 5386.
- [87] L. Huang, X. Chen, B. Bai, Q. Tan, G. Jin, T. Zentgraf, S. Zhang, *Light Sci. Appl.* **2013**, *2*, e70.

- [88] Q. Jiang, Y. Bao, F. Lin, X. Zhu, S. Zhang, Z. Fang, *Adv. Funct. Mater.* **2018**, *28*, 1705503.
- [89] J. Jin, X. Li, Y. Guo, M. Pu, P. Gao, X. Ma, X. Luo, *Nanoscale* **2019**, *11*, 3952.
- [90] D. Veksler, E. Maguid, N. Shitrit, D. Ozeri, V. Kleiner, E. Hasman, *ACS Photonics* **2015**, *2*, 661.
- [91] E. Maguid, I. Yulevich, M. Yannai, V. Kleiner, M. L. Brongersma, E. Hasman, *Light Sci. Appl.* **2017**, *6*, e17027.
- [92] M. Q. Mehmood, S. Mei, S. Hussain, K. Huang, S. Y. Siew, L. Zhang, T. Zhang, X. Ling, H. Liu, J. Teng, A. Danner, S. Zhang, C.-W. Qiu, *Adv. Mater.* **2016**, *28*, 2533.
- [93] D. Wen, S. Chen, F. Yue, K. Chan, M. Chen, M. Ardron, K. F. Li, P. W. H. Wong, K. W. Cheah, E. Y. B. Pun, G. Li, S. Zhang, X. Chen, *Adv. Opt. Mater.* **2016**, *4*, 321.
- [94] S. Choudhury, U. Guler, A. Shaltout, V. M. Shalae, A. V. Kildishev, A. Boltasseva, *Adv. Opt. Mater.* **2017**, *5*, 1700196.
- [95] L. Huang, H. Mühlenbernd, X. Li, X. Song, B. Bai, Y. Wang, T. Zentgraf, *Adv. Mater.* **2015**, *27*, 6444.
- [96] C. Zhang, F. Yue, D. Wen, M. Chen, Z. Zhang, W. Wang, X. Chen, *ACS Photonics* **2017**, *4*, 1906.
- [97] D. Wen, F. Yue, G. Li, G. Zheng, K. Chan, S. Chen, M. Chen, K. F. Li, P. W. H. Wong, K. W. Cheah, E. Yue Bun Pun, S. Zhang, X. Chen, *Nat. Commun.* **2015**, *6*, 8241.
- [98] J. P. Balthasar Mueller, N. A. Rubin, R. C. Devlin, B. Groever, F. Capasso, *Phys. Rev. Lett.* **2017**, *118*, 113901.
- [99] C. Zhang, S. Divitt, Q. Fan, W. Zhu, A. Agrawal, Y. Lu, T. Xu, H. J. Lezec, *Light Sci. Appl.* **2020**, *9*, 55.
- [100] R. C. Devlin, A. Ambrosio, N. A. Rubin, J. B. Mueller, F. Capasso, *Science* **2017**, *358*, 896.
- [101] S. Li, X. Li, G. Wang, S. Liu, L. Zhang, C. Zeng, L. Wang, Q. Sun, W. Zhao, W. Zhang, *Adv. Opt. Mater.* **2018**, *7*, 1801365.
- [102] S. Tian, H. Guo, J. Hu, S. Zhuang, *Opt. Express* **2019**, *27*, 680.
- [103] R. Jin, L. Tang, J. Li, J. Wang, Q. Wang, Y. Liu, Z. Dong, *ACS Photonics* **2020**, *7*, 512.
- [104] H. Xu, L. Han, Y. Li, Y. Sun, J. Zhao, S. Zhang, C. Qiu, *ACS Photonics* **2019**, *6*, 211.
- [105] Q. Fan, W. Zhu, Y. Liang, P. Huo, C. Zhang, A. Agrawal, K. Huang, X. Luo, Y. Lu, C. Qiu, H. J. Lezec, T. Xu, *Nano Lett.* **2019**, *19*, 1158.
- [106] P. Huo, C. Zhang, W. Zhu, M. Liu, S. Zhang, S. Zhang, L. Chen, H. J. Lezec, A. Agrawal, Y. Lu, T. Xu, *Nano Lett.* **2020**, *20*, 2791.
- [107] A. C. Overvig, S. Shrestha, S. C. Malek, M. Lu, A. Stein, C. Zheng, N. Yu, *Light Sci. Appl.* **2019**, *8*, 92.
- [108] W. Liu, Z. Li, Z. Li, H. Cheng, C. Tang, J. Li, S. Chen, J. Tian, *Adv. Mater.* **2019**, *31*, 1901729.
- [109] S. Chen, Z. Li, W. Liu, H. Cheng, J. Tian, *Adv. Mater.* **2019**, *31*, 1802458.
- [110] C. Meng, S. Tang, F. Ding, S. I. Bozhevolnyi, *ACS Photonics* **2020**, *7*, 1849.
- [111] M. Kauranen, A. V. Zayats, *Nat. Photonics* **2012**, *6*, 737.
- [112] M. Lapine, I. V. Shadrivov, Y. S. Kivshar, *Rev. Mod. Phys.* **2014**, *86*, 1093.
- [113] A. E. Minovich, A. E. Miroshnichenko, A. Y. Bykov, T. V. Murzina, D. N. Neshev, Y. S. Kivshar, *Laser Photonics Rev.* **2015**, *9*, 195.
- [114] G. Li, S. Zhang, T. Zentgraf, *Nat. Rev. Mater.* **2017**, *2*, 17010.
- [115] S. Keren-Zur, L. Michaeli, H. Suchowski, T. Ellenbogen, *Adv. Opt. Photonics* **2018**, *10*, 309.
- [116] B. Sain, C. Meier, T. Zentgraf, *Adv. Photonics* **2019**, *1*, 024002.
- [117] Z. Liu, Y. Xu, Y. Lin, J. Xiang, T. Feng, Q. Cao, J. Li, S. Lan, J. Liu, *Phys. Rev. Lett.* **2019**, *123*, 253901.
- [118] K. Koshelev, S. Kruk, E. Melik-Gaykazyan, J.-H. Choi, A. Bogdanov, H.-G. Park, Y. Kivshar, *Science* **2020**, *367*, 288.
- [119] Q. Wang, E. T. F. Rogers, B. Gholipour, C.-M. Wang, G. Yuan, J. Teng, N. I. Zheludev, *Nat. Photonics* **2016**, *10*, 60.
- [120] J. Tian, H. Luo, Y. Yang, F. Ding, Y. Qu, D. Zhao, M. Qiu, S. Bozhevolnyi, *Nat. Commun.* **2019**, *10*, 396.
- [121] F. Ding, Y. Yang, S. I. Bozhevolnyi, *Adv. Opt. Mater.* **2019**, *7*, 1801709.
- [122] A. Leitis, A. Heßler, S. Wahl, M. Wuttig, T. Taubner, A. Tittl, H. Altug, *Adv. Funct. Mater.* **2020**, *30*, 1910259.
- [123] S. Abdollahramezani, O. Hemmatyar, H. Taghinejad, A. Krasnok, Y. Kiarashinejad, M. Zandehshahvar, A. Alu, A. Adibi, *Nanophotonics* **2020**, *9*, 1189.
- [124] Y. Yao, R. Shankar, M. A. Kats, Y. Song, J. Kong, M. Loncar, F. Capasso, *Nano Lett.* **2014**, *14*, 6526.
- [125] J. van de Groep, J.-H. Song, U. Celano, Q. Li, P. G. Kik, M. L. Brongersma, *Nat. Photonics* **2020**, *14*, 426.
- [126] J. Park, J. Kang, S. J. Kim, X. Liu, M. L. Brongersma, *Nano Lett.* **2016**, *17*, 407.
- [127] G. Kafaie Shirmanesh, R. Sokhoyan, R. A. Pala, H. A. Atwater, *Nano Lett.* **2018**, *18*, 2957.
- [128] G. K. Shirmanesh, R. Sokhoyan, P. C. Wu, H. A. Atwater, *ACS Nano* **2020**, *14*, 6912.
- [129] J. J. Sautter, I. Staude, M. Decker, E. Rusak, D. N. Neshev, I. Brener, Y. S. Kivshar, *ACS Nano* **2015**, *9*, 4308.
- [130] S.-Q. Li, X. Xu, R. M. Veetil, V. Valuckas, R. Paniagua-Domínguez, A. I. Kuznetsov, *Science* **2019**, *364*, 1087.
- [131] J. Li, P. Yu, S. Zhang, N. Liu, *Nat. Commun.* **2020**, *11*, 3574.
- [132] Z. Shen, S. Zhou, X. Li, S. Ge, P. Chen, W. Hu, Y. Lu, *Adv. Photonics* **2020**, *2*, 036002.
- [133] L. Cong, P. Pitchappa, Y. Wu, L. Ke, C. Lee, N. Singh, H. Yang, R. Singh, *Adv. Opt. Mater.* **2017**, *5*, 1600716.
- [134] A. L. Holsteen, A. F. Cihan, M. L. Brongersma, *Science* **2019**, *365*, 257.
- [135] X. Duan, S. Kamin, N. Liu, *Nat. Commun.* **2017**, *8*, 14606.
- [136] J. Li, S. Kamin, G. Zheng, F. Neubrech, S. Zhang, N. Liu, *Sci. Adv.* **2018**, *4*, eaar6768.
- [137] Q. Ma, Q. R. Hong, G. D. Bai, H. B. Jing, R. Y. Wu, L. Bao, Q. Cheng, T. J. Cui, *Phys. Rev. Appl.* **2020**, *13*, 021003.
- [138] F. Zhang, X. Xie, M. Pu, Y. Guo, X. Ma, X. Li, J. Luo, Q. He, H. Yu, X. Luo, *Adv. Mater.* **2020**, *32*, 1908194.
- [139] D. Lu, J. J. Kan, E. E. Fullerton, Z. Liu, *Nat. Nanotechnol.* **2014**, *9*, 48.
- [140] G. M. Akselrod, C. Argyropoulos, T. B. Hoang, C. Ciraci, C. Fang, J. Huang, D. R. Smith, M. H. Mikkelsen, *Nat. Photonics* **2014**, *8*, 835.
- [141] M. Y. Shalaginov, V. V. Vorobyov, J. Liu, M. Ferrera, A. V. Akimov, A. Lagutchev, A. N. Smolyaninov, V. V. Klimov, J. Irudayaraj, A. V. Kildishev, A. Boltasseva, V. M. Shalae, *Laser Photonics Rev.* **2015**, *9*, 120.
- [142] S. K. H. Andersen, S. Kumar, S. I. Bozhevolnyi, *Nano Lett.* **2017**, *17*, 3889.
- [143] S. Bogdanov, M. Y. Shalaginov, A. Lagutchev, C.-C. Chiang, D. Shah, A. Baburin, I. Ryzhikov, I. Rodionov, A. V. Kildishev, A. Boltasseva, V. M. Shalae, *Nano Lett.* **2018**, *18*, 4837.
- [144] J. Liu, R. Su, Y. Wei, B. Yao, S. F. C. da Silva, Y. Yu, J. Iles-Smith, K. Srinivasan, A. Rastelli, J. Li, X. Wang, *Nat. Nanotechnol.* **2019**, *14*, 586.
- [145] H. Wang, H. Hai, T.-H. Chung, J. Qin, L. Xiaoxia, J.-P. Li, R.-Z. Liu, H.-S. Zhong, Y.-M. He, X. Ding, Y.-H. Deng, Q. Dai, Y.-H. Huo, S. Höfling, C.-Y. Lu, J.-W. Pan, *Phys. Rev. Lett.* **2019**, *122*, 113602.
- [146] Y. Kan, S. K. H. Andersen, F. Ding, S. Kumar, C. Zhao, S. I. Bozhevolnyi, *Adv. Mater.* **2020**, *32*, 1907832.
- [147] Y. Bao, Q. Lin, R. Su, Z. Zhou, J. Song, J. Li, X. Wang, *Sci. Adv.* **2020**, *6*, eaba8761.

- [148] T. Stav, A. Faerman, E. Maguid, D. Oren, V. Kleiner, E. Hasman, M. Segev, *Science* **2018**, 361, 1101.
- [149] K. Wang, J. G. Titchener, S. S. Kruk, L. Xu, H. P. Chung, M. Parry, I. I. Kravchenko, Y. H. Chen, A. S. Solntsev, Y. S. Kivshar, D. N. Neshev, A. A. Sukhorukov, *Science* **2018**, 361, 1104.
- [150] P. Georgi, M. Massaro, K.-H. Luo, B. Sain, N. Montaut, H. Herrmann, T. Weiss, G. Li, C. Silberhorn, T. Zentgraf, *Light Sci. Appl.* **2019**, 8, 70.
- [151] L. Li, Z. Liu, X. Ren, S. Wang, V.-C. Su, M.-K. Chen, C. H. Chu, H. Y. Kuo, B. Liu, W. Zang, G. Guo, L. Zhang, Z. Wang, S. Zhu, D. P. Tsai, *Science* **2020**, 368, 1487.
- [152] J. Wang, S. Paesani, Y. Ding, R. Santagati, P. Skrzypczyk, A. Salavrakos, J. Tura, R. Augusiak, L. Mančinska, D. Bacco, D. Bonneau, J. W. Silverstone, Q. Gong, A. Acín, K. Rottwitz, L. K. Oxenløwe, J. L. O'Brien, A. Laing, M. G. Thompson, *Science* **2018**, 360, 285.



Fei Ding received his Ph.D. degree in optical engineering from Zhejiang University, Hangzhou, China, in 2015. He was a postdoctoral fellow at Centre for Nano Optics at the University of Southern Denmark (SDU Nano Optics) in Denmark from 2015 to 2019. He is currently an assistant professor at SDU Nano Optics. His current research interests are in the areas of nanophotonics, metasurfaces, plasmonics, and quantum nanophotonics, with particular focus on innovative and extreme aspects of light-matter interaction at the nanoscale.



Shiwei Tang received his Ph.D. degree in physics from Fudan University, Shanghai, China, in 2014. He was a postdoctoral fellow at Fudan University from 2014 to 2015. He joined Ningbo University, Ningbo, China, in 2016, and was promoted to an associate professor, in 2019. His current research interests include metamaterials, microcavities, nanomaterials, plasmonics, and nanophotonics. He has authored and coauthored more than 60 publications in scientific journals.



Sergey I. Bozhevolnyi received his Ph.D. degree in quantum electronics from Moscow Institute of Physics and Technology (Russia), in 1981. He initiated experimental research in near-field optics at the Institute of Physics, Aalborg University (Denmark) in 1991, where he has been professor in 2003–2009 before moving to the University of Southern Denmark (SDU). He is currently a professor and head of Centre for Nano Optics at SDU, serving also as a chair of technical science at Danish Institute for Advanced Study (D-IAS). His current research interests include linear and nonlinear nano-optics and plasmonics, including plasmonic interconnects and metasurfaces.